Architecture and evolution of an extensionally-inverted thrust (Mt. Tancia Thrust, Central Apennines): geological, structural, geochemical, and K-Ar geochronological constraints

M. Curzi[1]*, L. Aldega[1], S. Bernasconi[2], F. Berra[3], A. Billi[4], C. Boschi[5], S. Franchini[1], R. Van der Lelij[6], G. Viola[7], E. Carminati[1,4]

1. Dipartimento di Scienze della Terra, Sapienza Università di Roma, P.le Aldo Moro 5, 00185, Roma, Italy

2. Geological Institute, ETH Zürich, Sonneggstrasse 5, 8092 Zürich, Switzerland

3. Università degli Studi di Milano, Dipartimento di Scienze della Terra, Via Mangiagalli 34, 20133 Milano, Italy

4. Consiglio Nazionale delle Ricerche, c.o. Dipartimento di Scienze della Terra, Università di Roma Sapienza, P.le Aldo Moro 5, 00185 Roma, Italy

5. Istituto di Geoscienze e Georisorse, Consiglio Nazionale delle Ricerche, Via Moruzzi 1, 56124 Pisa, Italy

6. Geological Survey of Norway, 7491 Trondheim, Norway

7. Dipartimento di Scienze Biologiche, Geologiche ed Ambientali – BiGeA, Università degli studi di Bologna, Via Zamboni 67, 40126 Bologna, Italy

*Corresponding author: manuel.curzi@uniroma1.it

Luca Aldega: luca.aldega@uniroma1.it
Stefano Bernasconi: stefano.bernasconi@erdw.ethz.ch
Fabrizio Berra: fabrizio.berra@unimi.it
Andrea Billi: andrea.billi@cnr.it
Chiara Boschi: c.boschi@igg.cnr.it
Stefania Franchini: stefania.franchini@uniroma1.it
Roelant van der Lelij: roelant.vanderLelij@ngu.no
Giulio Viola: giulio.viola3@unibo.it
Eugenio Carminati: eugenio.carminati@uniroma1.it

Fault inversion may lead to significant obliteration of the early tectonic structures, thus preventing to produce a straightforward interpretation of the complete fault kinematics and deformation history. We adopt a multidisciplinary approach to: 1) reconstruct the tectonic evolution through space and in time of the extensionally-inverted Mt. Tancia Thrust (Central Apennines, Italy); 2) understand the deformation mechanisms and the transition and reactivation of compressional structures during negative tectonic inversion; and 3) constrain the origin of fluids involved during tectonic processes. To this end, we combined: 1) detailed geological mapping and multiscale structural analysis; 2) illite-smectite paleothermal indicator; 3) C, O, and clumped isotopes on calcite mineralizations and 4) K-Ar dating of authigenic and/or syn-kinematic illite from the MTT fault rocks. Results show that shortening occurred between ~9 and ~7 Ma, under multiple events of fluid overpressure and shear ruptures involving fluids entrapped over long term within the host rocks. Post-compressive tectonic inversion occurred at ~3 Ma under fluid pressure fluctuations during shear events with an input of meteoric-derived fluids. Tectonic inversion is spatially confined within the first few metres below the thrust surface in a volume dominated by the partial overprinting, folding, transposition, and re-utilization of the earlier compressional fabric.

1. Introduction

Deformation in the upper crust is often heterogeneous and mostly localized along brittle faults. Faults and fault rocks may be weak compared to the surrounding host rock and are thus likely to accommodate repeated slip episodes over long times, particularly when assisted by fluids (e.g. Holdsworth et al., 1997; Sibson, 1995 and 2000; Holdsworth et al., 2001; Smith et al., 2017; Marchesini et al., 2019). Many studies on fault and fault rocks in the brittle crust have indeed highlighted that weakening is caused by several mechanisms. These include the development of fluid overpressure within the fault core (e.g. Ivnis et al., 1990; Byerlee, 1990; Sibson, 1990; Collettini et al., 2019; Marchesini et al., 2019), the presence of low-friction phases as clay minerals within the fault zone (e.g. Vrolijk and van der Pluijm, 1999; Moore and Rymer, 2007; Smeraglia et al., 2017; Collettini et al., 2019), and the possible planar anisotropies of fault rocks (e.g. Collettini et al., 2009; Tesei et al., 2014).

Thrust fault negative inversion by subsequent normal faulting has been documented in orogenic wedges, where post-compressive extensional tectonics often follows contraction (e.g. Migliorini, 1948; Malavieille, 1987; Ivnis et al., 1990; Faccenna et al., 1995). Fault inversion may lead to significant obliteration of the early tectonic structures and fabric, thus preventing or making particularly difficult producing a straightforward interpretation of the complete fault kinematics and deformation history. For this reason, and due to the seismogenic potential of faults within the upper crust, much effort has been invested into a better understanding of fault architecture, their deformation mechanisms (including tectonic inversion) as well as their kinematic evolution through time (e.g. Smith et al., 2011; Viola et al., 2013; Collettini, 2011; Balsamo et al., 2014; Torgersen and Viola, 2014; Torgersen et al., 2015a).

Slip on brittle faults can form gouge, which commonly consists of crushed rock fragments and authigenic synkinematic clay minerals. The composition of clay minerals in fault gouge is controlled mainly by the composition of the host rock and by the chemistry of circulating fluids. In particular, K-bearing clay minerals may neoform by hydration reactions at formation temperatures between 60°C and 250°C (Lyons and Snellenburg, 1971; Rutter et al., 1986; Kralik et al., 1987; Środoń, 1999). Many studies have documented the potential of K-Ar geochronology for dating authigenic and/or synkinematic fine-grained minerals, especially clays, in fault rocks (e.g., Clauer et al., 2013; Torgersen et al., 2015a; Viola et al., 2016 and 2018; Aldega et al., 2019). Unravelling brittle deformation history can therefore be challenging due to the difficulties to obtain geologically significant events from the obtained apparent ages. This is often complicated by: 1) partial or full resetting of radiogenic system by thermal diffusion (e.g. Zwingmann et al., 2004), 2) post-faulting alteration (Viola et al., 2013), and 3) contamination of samples by inherited mineral components from the host rocks (e.g. Pevear, 1999; Torgersen et al., 2015b). Despite these difficulties, it has been demonstrated the possibility to trace the temporal evolution of complex multiply-reactivated brittle faults by K-Ar dating of clay gouge coupled with structural, detailed fault architectural, and X-ray diffraction analyses (Zwingmann et al., 2004; Uysal et al., 2006; Torgersen et al., 2015a, 2015b; Scheiber and Viola, 2018; Viola et al., 2013, 2016, 2018).

Bigi (2006) described the superimposition of a late extensional tectonic fabric on the earlier compressional fabric in the fault rocks along Mt. Tancia Thrust (MTT, Central Apennines), one of the main structures of the Sabine thrust belt (Bollati et al., 2011), suggesting that the MTT was extensionally-inverted. In this paper, we expand the work by Bigi (2006) presenting K-Ar ages of syn-kinematic clay minerals in fault gouge from the extensionally-inverted MTT to constrain radiometrically the timing of its compressional and extensional history within the framework of the Apennines orogenic build-up and post-compressive extension. In particular, we integrate multiscale

structural analysis of the MTT with K-Ar dating of clay gouge, stable and clumped isotope analysis, cathodoluminescence of calcite veins and X-ray diffraction (XRD) of clay size fractions to: 1) reconstruct the complex tectonic evolution of the exhumed MTT; 2) understand the reactivation and transposition of compressional structures during late tectonic inversion; and 3) constrain the source of fluids involved in the MTT deformation history.

2.   Geological Setting

2.1 Central Apennines

The central-northern Apennine is a thin-skinned, NW-SE trending, late Oligocene-to-Present fold-and-thrust belt. The belt is the result of the W-directed subduction of the Adriatic lithosphere beneath the European Plate in the context of the convergence between Europe and Africa (Malinverno and Ryan, 1986; Doglioni et al., 1991; Carminati et al., 2010; Cosentino et al., 2010).

The tectonic evolution of the central-northern Apennine wedge has been controlled by the occurrence of a main regional decollement level corresponding to Triassic evaporites and dolostones (Burano Fm.; Bally et al., 1986), although thin-skinned and thick-skinned thrusting models were alternatively proposed for the tectonic evolution of the central Apennines (e.g. Mazzoli et al., 2005; Billi et al., 2006). The structure of the central Apennines is essentially the result of the superimposition of two tectonic processes, consisting in orogenetic (compressive) and post-orogenetic (extensional) deformations progressively migrating toward the Apennine foreland (toward E; Fig. 1a, b). Shortening began in the internal (western) portion of the wedge in the Upper Oligocene and was mainly accommodated by thrust faults which scraped off the sedimentary succession lying above the Adriatic plate (i.e., Meso-Cenozoic carbonates deposited both in shallow and deep-water environments and Cenozoic foredeep clastics; Cosentino et al., 2010; Fig. 1b). Extension and associated extensional basins (e.g. Terni, Rieti, L'Aquila and Fucino Basins) began as early as in the early Pliocene in the internal and axial part of the central Apennines, associated with the development of the Tyrrhenian back-arc basin (e.g. Cosentino et al., 2010). Normal faulting was locally accommodated by reactivation of previous thrust faults (e.g. D'Agostino et al., 1998; Pace et al., 2016; Lucca et al., 2019). This crustal thinning was also followed by widespread magmatism and significant hydrothermal fluids ascension along the Tyrrhenian side of the Apennines (Vignaroli et al., 2015, 2016). Between compressive and post-compressive (extensional) deformations, out-of-sequence thrusting has been also documented, in particular along the oblique Olevano-Antrodoco Fault (OAF; Fig. 1b), along which right-lateral shear occurred (e.g. Mattei et al., 1995). The Sabine thrust belt (Sabini Mts.) is located to the west of the OAF (Fig. 1a,b), where the Upper Triassic-Middle Miocene stratigraphic succession is made up of carbonates interleaved with several intervals

of bioclastic calcarenites. This succession deposited in a transitional environment between the Latium-Abruzzi carbonate platform and the Umbria-Marche pelagic basin (Castellarin et al., 1978; Cavinato et al., 1986; Corda and Mariotti, 1986; Cosentino and Parotto, 1992; Cosentino et al., 2010; Fig. 1b). Compressional deformation in the Sabine thrust belt began in the late Miocene with a maximum shortening oriented N85° (Corrado, 1995a). Such compressional regime originated Adriatic-verging compressional structures and induced the overthrtusting of the Umbria-Marche Basin (and its transitional environment) above the Latium-Abruzzi carbonate platform along the OAF (Cavinato et al., 1986; Corrado, 1995a; Mattei et al., 1995; Turtù et al., 2013). Along the frontal and oblique thrust ramps of the OAF, the Sabine thrust belt experienced a clockwise rotation of about 30-40° (e.g. Corrado, 1995a; Tavani et al., 2015). In post Messinian time, the Sabine thrust belt was affected by out-of-sequence thrusting in response of the reactivation in a strike-slip mode of the OAF (Corrado, 1995a; Mattei et al., 1995; Turtù et al., 2013). Strike-slip movement was also accomodated in the western portion of the Sabine thrust belt along the Sabina Fault (e.g. Alfonsi et al., 1991; Mattei et al., 1995; Fig. 1b). Finally, in Late Pliocene time, post-compressive oblique normal faulting and associated local negative inversion of suitably oriented thrust faults occurred (Faccenna et al., 1995; Cosentino et al., 2014). The Sabine thrust belt is presently bordered by the normal fault systems of the Tiber Valley (to the west) and Rieti (to the northeast) basins that are related to the late Pliocene extensional tectonics. These basins are filled by marine and continental deposits (Cavinato et al., 1989; Fig. 1b).

The Sabine thrust belt is composed by five thrust sheets (TS 1, 2, 3, 4, 5 from top to bottom) separated by N-S striking regional thrust faults. The thrusts are imbricated toward the east and thrust onto the Latium-Abruzzi thrust sheet in correspondence to the OAF (Fig. 1b, c; Cosentino and Parotto, 1986, 1992; Cosentino et al., 1993; Cosentino et al., 2014). The MTT is one of the most internal thrust faults of the Sabine thrust belt and juxtaposes TS2 (Lower Jurassic–lower Eocene sediments) above TS3 (Middle Jurassic–middle Miocene sediments; Fig. 1b,c). A fault-propagation folding model (Suppe and Medwedff, 1990) has been proposed to describe the geometry and kinematic evolution of the Sabine thrust belt and MTT (Cosentino and Parotto, 1992; Bigi, 2006).

2.2 Mt. Tancia area

The sedimentary succession exposed in the Mt. Tancia area has a thickness of about 900 m. From the bottom to the top, the succession is formed by 20-30 m thick Upper Jurassic cherty limestone (Calcari Diasprigni Fm.) and ~250 m of Upper Jurassic-Lower Cretaceous micritic limestone (Maiolica Fm.). The Upper Cretaceous to lower Eocene deposits are made up of limestone and marly limestone

ascribed to the Scaglia Bianca, Scaglia Rossa, and Scaglia Variegata fms. (about 450 m thick). The succession evolves to Eocene-lower Miocene marl and calcareous marl of the Scaglia Cinerea Fm. with a thickness of 100 m and to lower Miocene calcarenite with volcanoclastic layers of the Bisciaro Fm. (about 50 m).

This succession was deformed by the orogenic compression starting in the middle Miocene and producing an Adriatic-vergent thrust sheet (TS2 in fig. 1c) characterized by Lower Jurassic–lower Eocene deposits, which overly the Upper Cretaceous to lower Miocene rocks (TS3 in fig. 1c).

The MTT is a 20 km-long, N-S striking, E-vergent thrust fault bounding the TS2 and TS3 (Fig. 1c; Cosentino et al., 2014). A ca. 3000 m of reverse offset was estimated along the MTT (Bigi, 2006). The MTT hangingwall anticline consists of Lower Jurassic-Lower Cretaceous limestone (Corniola Fm.-Maiolica Fm.), whereas the Upper Cretaceous-Lower Miocene marl and marly limestone (Scaglia Group and Bisciaro Fm.) crop out in the footwall syncline (Cosentino et al., 2014, Bigi, 2006). The MTT is well exposed in the southern flank of the Mt. Tancia, where the thrust fault juxtaposes the Maiolica Fm. onto the Scaglia Variegata Fm. The ~200 m thick shear zone is well developed in the footwall, where the cherty marly limestone and marl of the Scaglia Group (Scaglia Rossa, Scaglia Variegata, and Scaglia Cinerea Formations) are extremely deformed from the meso-down to the micro-scale, showing pervasive top-to-the ENE S-C/C' fabrics. Furthermore, the upper portion of the shear zone recorded an extensional inversion of the MTT, as testified by the superimposition of S-C/C' tectonic fabric with a top-to-the W-SW sense of shear (Bigi, 2006).

3. Methods

To reconstruct the tectonic evolution of the exhumed MTT, we combined different methods (see supplementary material for detailed description) including:

1) 1:5,000 scale geological mapping of an area of about 15 km^2 on the basis of the published geological map "Cittaducale" at a 1:50.000 scale (Servizio Geologico d'Italia);

2) Sampling and detailed meso-structural analyses both in the hangingwall and in the footwall of the MTT;

3) Laboratory microstructural analyses using a high-resolution scanner as well as optical and scanning electron microscopy;

4) Cathodoluminescence microscopy (CL);

5) Geochemical analyses of stable and clumped isotopes;

6) X-ray diffraction (XRD) analysis of the clay size fraction of the Eocene-Miocene succession and the fault gouge;

7) K-Ar dating of syn-kinematic clay minerals;

Moreover, we acknowledge that we performed in situ U-Pb dating on eight samples of calcite veins and two samples of calcite slickenfibers sampled within the shear zone and along the thrust surface of the MTT. The U-Pb geochronology was attempted at the laboratory of the Institute of Geosciences, Johann Wolfgang Goethe-University, Frankfurt am Main (Germany) following standard methods fully described in Ring and Gerdes (2016). Samples were pre-screened to identify sub-zones with high $^{238}U/^{206}Pb$ ratio to perform the analytical session. Unfortunately, given the very low amount of U and Pb in such calcite mineralizations (i.e. less than the detection limits of ~0.1 ppb for ^{206}Pb and 0.03 ppb for ^{238}U), successful measurements were not carried out.

4. Results

4.1 Geological Mapping and mesoscale structural analysis

At the kilometre-scale, the study area is characterized by the MTT, two splays, an hangingwall anticline, and a footwall syncline (Figs. 2 and S1). Looking from south to north, metric-scale parasitic Z-shaped folds with NNW-SSE striking and WSW dipping (20°-50°) axial planes are present both in the backlimb of the hangingwall anticline (Maiolica Fm.; Figs. 3a) and in the upright limb of the footwall syncline (Scaglia Cinerea Fm.). Sets of calcite veins locally occur in the limbs and hinge zones of these parasitic folds and are mainly subparallel (N 70°-90° striking) or orthogonal (N 130°-140° striking) to the fold axes (Fig. S2).

The footwall syncline, cored by the lower Miocene Bisciaro Fm., is NE-vergent with a NNW-SSE trending axis and an asymmetric profile (with a steep overturned westward-dipping limb and a shallow upright westward-dipping limb; Fig. 2). Toward the east, the footwall succession is also deformed by an open-gentle anticline (Fig. 2).

In the study area, we observed evidence of strike-slip tectonics along WNW-ESE oriented faults displacing the footwall succession and locally the MTT (SW in Fig. 2). Left-lateral transtensional movement is particularly evident in the central portion of the map (Fig. 2), where the older formation in the footwall is exposed (Scaglia Bianca Fm., Upper Cretaceous) in the core of the open-gentle anticline.

Two splay thrusts complicate the footwall succession. One splay juxtaposes the Scaglia Variegata Fm. (Eocene) onto the Scaglia Cinerea Fm. (upper Eocene-lower Miocene) and crops out in the northern and central portions of the map (Fig. 2). The other splay is exposed both in the central portion of the map (Fig. 2), with the tectonic contact between the Scaglia Rossa Fm. (above, Upper

Cretaceous-middle Eocene) and Scaglia Variegata Fm. (below, Eocene), and in the south-eastern area (Fig. 2), where a klippe of the Scaglia Rossa Fm. rests above the Scaglia Cinerea Fm. (upper Eocene-lower Miocene).

The MTT shear zone has a thickness of about 150-200 m (Fig. 3a) and is mostly developed in the footwall, where the marly limestone of the Scaglia Rossa, Scaglia Variegata, and Scaglia Cinerea fms. exhibit pervasive S-C/C' fabrics. The different rheological behaviour of the marly and calcareous layers of the Scaglia facies Formations and their calcarenite intercalations is highlighted by the different intensity and distribution of tectonic fabric (Fig. 4). The less competent marly horizons are deformed by closely spaced (c. 0.5-1.5 cm) S and C planes (Fig. 4). The mostly calcareous portions are deformed by widely spaced (between 5-10 cm) S and C planes delimiting portions of undeformed host rock (lithons) at the outcrop scale (Fig. 4a). The competent calcarenite levels are not affected by pressure-solution deformation and have rigid behaviour as testified by local bookshelf structures (Fig. 4b).

Within the shear zone, superimposed S-C/C' fabrics with contrasting kinematics indicate the superposition of different motions along the MTT. The old S-C/C' fabric (K1 fabric) is widely exposed in most of the shear zone and constrains a top to-ENE reverse sense of shear (Fig. 5). In detail, the K1 fabric is characterized by NNW-SSE striking and WSW (10°-45°) dipping dissolution S planes. C planes strike NNW-SSE, dip 20°-50° toward WSW, and are characterized by the occurrence of calcite slickenfibers indicating a top-to-E-NE thrusting. C' planes are less common, strike NE-SW, and mainly dip toward W-NW by ~45° (Fig. 5c). The superimposed younger S-C/C' fabric (K2 fabric) is exposed in the central portion of the area (see structural sites 6 and 9 in figure 2), and it is limited to the first few metres below the thrust surface, where the Scaglia Variegata Fm. crops out. This fabric consists of NE dipping (5°-40°) dissolution S planes, WSW dipping (20°-50°) C planes decorated by calcite slickenfibers indicating a top-to-WSW extensional faulting, and less common WSW dipping (30°-80°) C' planes.

The best exposure of the MTT can be osbserved in the central portion of the study area (see structural site 9 in Figs. 2, 3 and 6a). Here, the thrust dips to the W (20°-45°) and juxtaposes limestone of the Maiolica Fm. (Upper Jurassic-middle Cretaceous) against the intensely foliated marly limestone of the Scaglia Variegata Fm. (Eocene) (Fig. 6a). A system of NE-SW striking left-lateral transtensional faults offsets the thrust surface with a maximum displacement of 40-50 cm (Fig. 6a). Such transtensional faults occur also in the footwall as high-angle-low-displacement oblique-normal faults and low-angle-low-displacement oblique-normal faults (Fig. 6a).

Within the hangingwall, lenses of brecciated limestone of the Maiolica Fm., arranged in a metric-scale imbricate structure, are bounded by smooth, low-displacement shear surfaces characterized by evidence of extensional inversion (Fig. 6e). These lenses are observed in correspondence of a metric-scale thrust ramp.

Grooves and slickenlines on the thrust surface indicate dip-slip and strike-slip (both left- and right-lateral) movements (Fig. 6c). Calcite slickenfibers are less common and evidence of crosscutting relationships indicates that the last fault slip occurred with a dip-slip (70°-90°) normal sense of shear (Fig. 6d and see plot in Fig. 6a).

In the outcrop shown in Fig. 6a, the pervasive S-C/C' fabric indicates extensional top-to-WSW movement (K2 fabric) with C and C' planes dipping toward WSW and dissolution S planes dipping toward NE (5°-40°) (Fig. 6b). This fabric extends more than 5 m in the footwall right below the thrust surface. The gently dipping (5°-20°) S planes are also characterized by small and localized calcite slickenfibers on the dissolved surfaces indicating that these structures were used also for shear displacement (see Schmidt diagram in Fig. 6b). The K2 fabric is associated with the extensional inversion of the MTT and reveals a substantial overprinting but also, in places, a partial re-use of K1. Owing to the parallelism between C planes of K1 and K2 fabrics, such shear planes were inverted extensionally during the negative inversion of the MTT. Moreover, folding of the K1 fabric is commonly observed (Fig. 7), locally associated with a crenulation cleavage (Fig. 6f).

4.2 Microstructural analysis

The MTT fault rocks are deformed by pervasive pressure-solution and frictional sliding producing S-C/C' fabrics, containing microdomains with distinct deformation styles.

1) *Tectonites with a top-to-ENE reverse sense of shear (K1 fabric)*

The more competent portions of the tectonites are mainly formed by spaced dissolution planes and are affected by abundant 2-6 mm thick calcite veins oriented parallel and perpendicular with respect to the S planes (Fig. 8a). The marly portions represent the high-strain microdomains and are intensely foliated by parallel and closely spaced dissolution S planes, which include insoluble materials. These planes locally surround planktonic foraminifera which are preserved or only partially dissolved by S planes, therefore representing rheological barriers at the microscale (Fig. 8b).

Variously-oriented calcite veins with a blocky texture are present. Mutual cross-cutting relationships between such veins and dissolution planes exist (Fig. 8d). Calcite veins disposed along S planes (Fig. 8a, b, c, e, f) are commonly deformed by dissolution planes that localize along the vein margins or

into the veins themselves (Fig. 8f). Such veins are also locally affected by boudinage developed through synthetic shear planes (C' planes) forming sigmoidal blocks (Fig. 8e).

Some calcite veins bound the poorly-to-non-foliated sigmoidal calcareous blocks with a relative rigid mechanical behaviour that are locally packed into the marly-highly-foliated portions (Fig. 8a, b, d).

All the calcite veins are characterized by cements which appear homogeneously dull under cathodoluminescence light (CL), showing no zonation (Fig. 9a, b, c). Despite the general similarity among the calcite veins, some are darker (Fig. 9c): these veins are cut by later fractures (filled by calcite dark in cathodoluminescence), whereas the lighter dull veins do not show clear fractures. Under the optical microscope, intracrystalline plastic deformation of all calcite veins is indicated by undulose extinction and mechanical deformation twinning.

Mineralizations along C planes are composed of millimetric slices of host rock interlayered with multiple subparallel twinned blocky calcite veins bounded by scabrous (or teeth-shaped) dissolution planes (Fig. 8g, 10a). Evidence of shear along C planes is rarely observed by multiple subparallel inclusion bands with micrometer-thick separations disposed at high angle (~70°) to the sharp shear planes (Fig. 10b). Blocky veins and calcite slickenfibers do not show different colours (dull red) under CL light (Fig. 10c).

2) Tectonites with folded S-C/C' fabric (deformed K1 fabric)

S planes, calcite veins, and host rock relicts are widely deformed by disharmonic folds, characterized by variable wavelength, symmetry, and shape (Fig. 11a,b). Calcite veins are passively rotated during folding (Fig. 11b) and en-échelon calcite veins with blocky texture are locally bounded by dissolution planes (Fig. 11c). Some calcite veins display fibrous habitus, which testifies for micrometer-thick growth increments (Fig. 11d). Such mineralizations developed parallel to the normal shear sense and are bounded by S planes.

3) Tectonites with a top-to-WSW sense of shear (K2 fabric)

The more calcareous portions of the fault rocks are characterized by anastomosed S planes indicating WSW-directed shear, which bound calcareous sigmoidal lithons and calcite mineralizations (Fig. 12a). Such planes are also tightly crenulated (Fig. 12a). C' planes are locally developed at a low angle with respect to the thrust surface (Fig. 12a). Along such planes, blocky calcite veins with sharp boundaries and fibrous calcite mineralizations are bounded by teeth-shaped dissolution planes (Fig. 12b).

Calcite veins mainly occur within the more competent (calcareous) portions of the tectonites, where microfossils are well preserved and only minor internal deformation is observed (Fig. 12c).

The less competent (marly) portion of the fault rocks is characterized by closely spaced S planes bounding calcite mineralizations and calcareous sigmoids (Fig. 12d, e). Such calcareous sigmoidal lithons are internally deformed by folded S planes of K1 fabric truncated by S planes of K2 fabric (Fig. 12d,e). Fibrous calcite locally occurs (Fig. 12f) and calcite veins of the K1 fabric are well preserved in the less foliated calcareous portions (Fig. 12e). Elongated and stretched calcite veins bounded by dissolution planes and oriented parallel to the dissolution surfaces of K1 fabric are locally present (Fig. 12d).

Rocks above the thrust surface are characterized by brecciated texture, dissolution planes, and calcite veins. Such calcite veins show mutual cross-cutting relationships and are locally cut by dissolution planes (Fig. S3a). The principal slip zone (PSZ) has a thickness of about 50-100 µm and appears essentially altered under the optical microscope (Fig. S3a). Furthermore, spectrometer energy dispersive (EDS) chemical maps highlight the concentration of Al, Fe, Mg, P, and Si into the PSZ (Fig. S4). Scanning electron microscope (SEM) observations show porous domains with flame-like structures along and just above the PSZ (Fig. S3b). As shown in Figs. S3b and S3c, these domains are likely to represent dissolved portion of the host rock characterized by high concentration of Ca (~60 wt. %) ad S (~35 wt. %) (Fig. S5a). SEM observations and chemical analyses highlight also the occurrence of cubic sylvite (KCl) crystals (Fig. S3d,e, S5b) and Ca-rich baryte mineralizations (Fig. S3d and S5c) above the PSZ.

4.3 X-ray diffraction of the Mt. Tancia sedimentary succession and fault gouge

We collected five samples from the marls of the Scaglia Variegata and Scaglia Cinerea fms. and from calcarenites of the Bisciaro Fm. at the footwall of the MTT in order to reconstruct the maximum overburden experienced by the sedimentary succession (Fig. 2 for sampling location).

The results of the X-ray semiquantitative analysis of the <2µm grain-size fraction of sediments are shown in Table 1. The Scaglia Variegata Fm. is characterized by illite and mixed layers illite-smectite (I-S) -rich composition with very low amounts of chlorite (3%). In the Scaglia Cinerea Fm., illite is the most abundant clay mineral with contents of 48-55% followed by mixed layers I-S (38-40%) and subordinate amounts of chlorite ranging from 5 to 14%. The calcarenites of the Bisciaro Fm. have a clay mineral assemblage similar to that observed in the Scaglia Cinerea Fm. (Tab.1). Mixed layers I-S are disordered structures with an illite content that slightly increases as a function of the stratigraphic age from 40% to 50%. The composition of mixed layer I-S suggests that the sedimentary succession experienced low levels of thermal maturity in early diagenetic conditions (Corrado, 1995b; Corrado, et al., 2010; Merriman and Frey, 1999; Aldega et al., 2007).

Table 1: Semiquantitative X-ray diffraction analysis of the <2μm grain-size fractions for the Eocene-early Miocene succession exposed at Mt. Tancia.

I-illite; I-S-mixed layer illite-smectite; Chl-chlorite; Qtz-quartz; Cal-calcite; Zeo-zeolite minerals.

Sample ID	Formation	<2 µm grain size fraction (%wt)					
		I	I-S	Chl	Other	R	%I in I-S
3	Bisciaro Fm.	51	32	17	Qtz+ Cal+Zeo	0	40
4	Scaglia Cinerea Fm.	55	40	5	Qtz+ Cal	0	40
9	Scaglia Cinerea Fm.	48	38	14	Qtz+ Cal	0	45
1	Scaglia Variegata Fm.	49	51	-	Qtz+ Cal	0	50
2	Scaglia Variegata Fm.	57	40	3	Qtz+ Cal	0	50

We collected three fault gouge samples from the MTT. In detail, we collected two samples from structural site 1, where a clear reverse kinematics is observed (K1 fabric; samples MC91 and MC92; Fig. 13b, c and Fig. 2 for locations), and one sample from structural site 7, where extensional K2 fabric overprints the compressional K1 fabric (MC90; Fig. 13a and Fig. 2 for location). We collected samples MC91 and MC92 at the footwall of the MTT, near the thrust splay exposed at structural site 7. There, the thrust splay juxtaposes the Scaglia Variegata Fm. onto the Scaglia Cinerea Fm. (Fig. 2 for location). Eleven sub-fractions (from <0.1 to 10 µm) from gouges formed at expense of the Scaglia Variegata Fm. (samples MC90 and MC91) and Scaglia Cinerea Fm. (MC92) were analyzed for illite polytype determinations and X-ray semiquantitative analysis (Fig. 14a and Tab. S1). This allowed us to discriminate between authigenic/synkinematic illite crystals (illite-1M_d polytype) formed during faulting and protolithic illite crystals (illite-2M_1 polytype) inherited from the host rock.

The mineralogical assemblage of the clay gouge samples preserving the K1 fabric (MC91 and MC92) mainly consists of calcite, quartz, illite/muscovite-2M_1, illite-1M_d, random ordered mixed layers I-S, chlorite, and plagioclase (Fig. 14a).

Calcite is particularly abundant in the coarse subfractions (0.4-2 µm, 2-6 µm, 6-10 µm) with contents between 51 and 89% but progressively decreases in the finer fractions (<0.1 µm, 0.1-0.4 µm,) with percentages between 4 and 12%. Quartz content decreases slightly with the decreasing grain size

(about 11-16% in the coarse fractions and <9% in the finer fractions). Plagioclase occurs in the 0.4-2 µm, 2-6 µm, and 6-10 µm fractions with contents <4% whereas chlorite does not exceed 3% in any of the subfractions. The decrease in content of the non-clay minerals in the fine fractions is compensated by the neoformation of illite-$1M_d$ and illite/muscovite-$2M_1$. Illite-$1M_d$ increases from 1-5% in the coarse subfractions to 19-24% in the finer subfractions. Analogously, illite/muscovite-$2M_1$ increases from 2-6% to 8-14% from the coarse to the fine subfractions. Mixed layer I-S is the dominant clay mineral in the <0.1 µm fractions forming at least 50% of the whole-rock mineralogical assemblage (Fig. 14a and Tab. S1).

The clay gouge sample with the K2 fabric (MC90, Scaglia Variegata Fm.) has a clay mineral assemblage similar to that previously described for the K1 fabric with a progressive increase of illite-$1M_d$ and illite/muscovite-$2M_1$ contents as a function of the decreasing grain size (Fig. 14a and Tab. S1). Mixed layer I-S occurs only in the <0.1 µm and 0.1-0.4 µm fractions with contents ranging between 26% and 29%.

4.4 K-Ar ages

We analysed five subfractions for each of the 3 samples (MC90, MC91, MC92) dated in this study (Table 3).

Table 3: K- Ar data for the gouge samples of the MTT

Sample ID	Grain-size fraction (µm)	K Mass mg	K wt %	K σ (%)	$^{40}Ar^*$ Mass mg	$^{40}Ar^*$ mol/g	$^{40}Ar^*$ σ (%)	$^{40}Ar^*$ %	Age Data Age (Ma)	Age Data σ (Ma)
MC 90	<0.1	51.4	3.474	1.5	4.672	2.3032E-10	0.29	17.8	37.8	0.6
MC 90	0.1-0.4	51.4	3.545	1.5	4.576	3.4567E-10	0.26	26.6	55.4	0.9
MC 90	0.4-2	56.8	3.402	1.5	4.482	4.4045E-10	0.25	36.4	73.1	1.1
MC 90	2-6	57.7	2.469	1.5	3.532	3.5580E-10	0.28	41.5	81.2	1.2
MC 90	6-10	50.4	1.812	1.5	2.774	2.5202E-10	0.36	40.2	78.5	1.2
MC 91	<0.1	7.1	2.901	2.1	1.356	2.7720E-10	0.59	35.1	54.3	1.1
MC 91	0.1-0.4	51.9	3.001	1.5	2.918	4.5790E-10	0.29	39.0	85.9	1.3
MC 91	0.4-2	53.0	2.525	1.5	4.220	5.0548E-10	0.25	49.5	111.9	1.7

MC 91	2-6	51.4	1.690	1.5	3.858	4.0987E-10	0.27	59.5	134.7	2.0
MC 91	6-10	54.8	1.429	1.5	3.650	3.4853E-10	0.28	60.8	135.4	2.0
MC 92	<0.1	22.7	3.515	1.6	3.048	3.1913E-10	0.32	26.2	51.6	0.9
MC 92	0.1-0.4	54.7	3.385	1.5	3.666	4.5898E-10	0.27	39.2	76.5	1.1
MC 92	0.4-2	54.0	2.903	1.5	4.172	5.4043E-10	0.25	49.7	104.3	1.5
MC 92	2-6	57.7	1.781	1.5	4.006	4.2767E-10	0.26	63.4	133.4	1.9
MC 92	6-10	54.0	1.230	1.5	2.850	2.7163E-10	0.34	65.4	123.1	1.9

For all the samples, a general direct grain size-age correlation occurs, wherein the coarser the dated grain size fraction, the older the age (Fig. 14b, Tab. 3). From the finer to the coarser fractions, sample MC90 yields K-Ar dates between 37.8 ± 0.6 Ma and 78.5 ± 1.2 Ma (Tab. 3), sample MC91 yields K-Ar dates between 54.3 ± 1.1 Ma and 135.4 ± 2.0 Ma (Tab. 3), and sample MC92 yields K-Ar dates between 51.6 ± 0.9 Ma and 123.1 ± 1.8 Ma. The ages of the finest fractions, which are older than the depositional age (Eocene-lower Miocene) of the host rocks (Tab. 3), suggest a mixing between syn-kinematic and authigenic illite and detrital illite inherited from the host rock. We assessed the effects of potential host rock contamination by protolithic illite through the Illite Age Analysis approach (IAA; e.g. Pevear, 1999). The IAA discriminates between the mostly detrital $2M_1$ polytype (which, in turn, may represent a mixture of authigenic high-temperature illite and cataclastic, synkinematic muscovite) and a truly authigenic phase $1M_d$ formed during brittle faulting. To estimate the age and uncertainty of authigenic/synkinematic illite-$1M_d$ and detrital illite-$2M_1$, we normalized to 100% the proportion of illite-$2M_1$ and illite-$1M_d$ determined by XRD analysis plotting the data as apparent K-Ar date vs. percentage of detrital illite, and linearly extrapolated to 0 and 100% illite-$2M_1$ by ordinary least square regression. By means of this ordinary least square regression, the age of the last slip event recorded by MC90 is at 2.9 ± 7.0 Ma, by MC91 is at 7.3 ± 25.5 Ma, and by MC92 is at 9.3 ± 14.9 Ma (Fig. 14c). The age of the regressed detrital illite-$2M_1$ recorded by sample MC90 is 152.4 ± 9.8 Ma, by sample MC91 is 201.1 ± 20.5 Ma, and by sample MC92 is 190.5 ± 16.1 Ma (Fig. 14c). Thus, the illite-2M1 polytype represents a detrital contamination from the host rocks to the fault gouge as all the regressed IAA ages are older than the depositional ages (Eocene-lower Miocene) of the host rocks.

4.5 Stable and clumped isotopes

Results from stable isotope analyses are shown in Fig. 15 and listed in Table S2. Results are reported in the conventional δ notation with respect to the Vienna Pee Dee Belemnite (VPDB) for $\delta^{13}C$ and Vienna Standard Mean Ocean Water (VSMOW) for $\delta^{18}O$.

The host rock (Maiolica , Scaglia Variegata and Scaglia Cinerea fms.) $\delta^{13}C$ and $\delta^{18}O$ values range between +1‰ and +1.7‰, and between +29.5‰ and +30.6‰, respectively. These values are typical for Meso-Cenozoic carbonate marine deposits in the central Apennines (e.g., Ghisetti et al., 2001; Agosta and Kirschner, 2003).

Calcite veins collected in the limbs and hinge zones of parasitic folds at the hangingwall of the MTT (Maiolica Fm.) display $\delta^{13}C$ and $\delta^{18}O$ values between +1.3‰ and 1.5‰, and between +25.7‰ and 28.7‰, respectively (Fig.15).

Calcite veins (both variously oriented and along shear C planes) sampled within fabric K1 from 50 m to 150 m below the thrust surface (Scaglia Variegata and Scaglia Cinerea fms.) show a narrow range of values for $\delta^{13}C$ between +1.3‰ and 1.6‰, and for $\delta^{18}O$ between +28.4‰ and 30‰ (Fig.15). Calcite veins sampled along C planes of K2 fabric exposed in the first meters below the thrust surface are characterized by $\delta^{13}C$ values between +1.4‰ and 1.7‰ and by a large range of $\delta^{18}O$ values between 22.9‰ and 29.7‰ (Fig.15).

Clumped isotopes are reported in the carbon dioxide equilibration scale (CDES) with temperature uncertainty at the 95% confidence level. Clumped isotope data from one calcite vein within the K1 fabric and one calcite vein within the K2 fabric yield Δ_{47} values between 0.537‰ and 0.584‰ and between 0.661‰ and 0.670‰, respectively (Tab. S3). Clumped isotope data from three footwall host rock samples (Scaglia Variegata Fm.) yields Δ_{47} values between 0.592‰ and 0.638‰ (Tab. S3). Using a revised version of the Kele et al. (2015) calibration (see Methods in the supplementary material), these values correspond to temperatures between $55 \pm 2.4°C$ and $78 \pm 26.5°C$ for the calcite vein within the K1 fabric, between $28 \pm 4.3°C$ and $26 \pm 7.3°C$ for the calcite vein within the K2 fabric, and between $\sim 36 \pm 11.7°C$ and $\sim 55 \pm 24.8°C$ for the footwall host rock samples (Scaglia Variegata Fm.; Fig. 15 and Table S3).

5. Burial history

The simplified reconstruction of the Eocene-Miocene sedimentary succession deformed by the MTT was performed using the software package Basin Mod-1D and was constrained by K-Ar IAA ages of syn-kinematic illite, which provided time constraints for thrusting and extensional faulting, and by randomly oriented I-S, which provided the paleothermal constraint.

The main assumptions for modelling are: (i) rock decompaction factors apply only to clastic deposits (Sclater & Christie, 1980), (ii) thermal evolution is mainly affected by sediment thickness rather than by paleowater depth, and (iii) variable geothermal gradient is adopted. We used 30 °C/km during wedge accretion (Allen & Allen, 2013) in Miocene-Pliocene time, 20 °C/km during tectonic inversion of the MTT in late Pliocene time, and 20 °C/km as the present-day geothermal gradient (Della Vedova et al., 1991). The thickness of the Eocene-Miocene sedimentary succession was calculated from field mapping and geological cross sections. We converted the illite content in mixed layers I-S into vitrinite reflectance-equivalent values using the correlation of vitrinite reflectance and expandability data based on the kinetic model of vitrinite maturation (Burnham & Sweeney, 1989) and on the kinetics of the I-S reaction (Hillier et al., 1995).

Figure 16 shows that, after the deposition of 200 m thick limestones, marls, and turbidites during the Eocene and the middle Miocene, the sedimentary succession was buried at depth of about 2000 m by a ~1700 m-thick thrust stack. In detail, maximum burial occurred during the upper Tortonian at 7.35 Ma, when the Eocene-Miocene succession experienced early diagenetic conditions, with maximum temperature of ~70 °C. During the tectonic burial, the fabric K1 developed in the footwall. Levels of thermal maturity experienced by the sedimentary succession (Fig. 16b) are consistent with low vitrinite reflectance values recorded by several tectonic units in the central-northern Apennines (e.g. Corrado, 1996, Corrado et al., 2010; Caricchi et al., 2015a, b). The modeled thrust sheet consists of part of TS2 (~650-700 m) and the overlapping thrust sheet TS1 (with a thickness of ~1000-1050 m), as described in Cosentino et al. (2014; Fig. 1c). TS1 is nowadays mostly eroded and only partially exposed in the western Sabine thrust belt to the northeast of the study area (Fig. 1c). Since late Pliocene time (K-Ar IAA age of 2.88 Ma), the Eocene-Miocene sedimentary succession exhumed at a constant rate of 0.59 mm/yr driven by footwall isostatic rebound and the ~1700 m thrust stack began to be eroded as result of post-compressive extensional tectonics, when the K2 developed and the MTT was inverted and locally cut by transtensional faults.

6. Discussion

6.1 Rationale

To reconstruct the architecture and the spatial-temporal tectonic evolution of the MTT, we first discuss the results obtained by K-Ar dating. Then, based on our multiscale structural observations and analytical results, we discuss the complex architecture and evolution of the whole structure of the MTT in terms of fluid-assisted compressive and post-compressive deformation mechanisms and rheological behaviour.

6.2 K-Ar geochronological constraints

In the western Sabine thrust belt, the youngest pre-orogenic (Schlier Fm., ~20-13 Ma) and syn-orogenic deposits (Marnoso Arenacea Fm. ~11-5 Ma) are rarely and only partially exposed (Cosentino et al., 2014). For this reason, temporal constraints upon the tectonic evolution of the western Sabine thrust belt are frequently inferred by stratigraphic and biostratigraphic data from surrounding areas. In detail, an upper Serravallian-upper Tortonian age (ranging from about 13 to 7 Ma) has been proposed for compressional tectonics whereas a Pliocene-lower Pleistocene age (between about 5 and 1 Ma) has been proposed for post-compressive extensional tectonics (Cipollari and Cosentino, 1996; Cipollari et al., 1997; Cosentino et al., 2014). Our K-Ar ages represent the first data that radiometrically constrain timing of compressional (orogenic) and extensional (post-compressive) deformation in this sector of the belt. The direct grain size-age correlation for the dated samples (MC90, MC91, and MC92; Fig. 14b) is interpreted as the result of mixing between detrital illite-$2M_1$ inherited from the host rock and authigenic and/or synkinematic illite- $1M_d$ formed during the latest recorded increment of faulting at low temperature (e.g. Pevear, 1999). The K-Ar date of the finest fraction is considered to be the closest to the age of the last recorded faulting episode, when syn-kinematic illite growth is mostly recorded by the finest fraction. However, the date of the finest fraction might still represent a mixed age, partially reflecting the isotopic contribution of K-bearing minerals reworked from the host rock into the fault gouge during cataclasis.

When dealing with absolute K-Ar geochronology on syn-kinematic clay minerals in fault gouge formed at expense of rocks with terrigenous components, mixing between inherited and syn-kinematic K-bearing minerals cannot always be completely identified and unraveled by Illite Age Analysis (IAA). The absolute K-Ar IAA ages (Fig. 14c) are coherent with some independent geological (biostratigraphic and stratigraphic) time constraints available for the western Sabine thrust belt (Cavinato and De Celles, 1999; Cosentino et al., 2014; Fig.17). On the basis of IAA results, illite-$1M_d$ formed during a thermotectonic event occurred in the 9.35-7.35 Ma time span. Considering the large errors associated with the K-Ar age, a more speculative interpretation of the radiometric ages would imply two thermotectonic events, the first occurred at 9.35 Ma (middle Tortonian) and the second at 7.35 Ma (upper Tortonian), with a minimum duration of 2 Ma for the compressional tectonics. Considering both our reconstruction of the MTT and our sampling locations, the younger age (7.35 Ma) could correspond to the development of the two splays in the late stages of the compressional evolution, when the footwall succession experienced the maximum tectonic burial (see the following section). Finally, the IAA age resulting from MC90 suggests that tectonic inversion

occurred at 2.88 Ma (Late Pliocene), implying that the lag time between the end of thrusting and the beginning of extensional tectonics was about 4.5 Ma long (between 7.35 Ma and 2.88 Ma).

6.3 Compressional evolution of the MTT

During the compressional orogenic stage, NW-SE trending hangingwall anticline and footwall syncline developed progressively in the Mt. Tancia area at the tip of the propagating MTT (Fig. 18a), according to the "fault-propagation folding" kinematic model (Suppe and Medwedeff, 1990). This model was previously suggested for the MTT by Bigi (2006). Our structural field measurements of the exposed thrust surface are consistent with model prediction of a gently dipping propagating thrust fault (< ~35°-40°) associated with a gently inclined hangingwall anticline (Fig. 18b; Davis et al., 2011). The youngest pre-orogenic deposits (~20 m thick shales and marls of the Schlier Fm.) described in the western Sabine thrust belt are early-middle Miocene in age (Cosentino et al., 2014), whereas in the study area the youngest deposits consist of the early Miocene Bisciaro Fm. exposed in the core of the footwall syncline (Fig. 18b). For this reason, we speculate that the removal by lateral flow of ~20 m thick shales and marls occurred in association with folding during compressional tectonics. The lateral flow of plastic material, as the Schlier Fm., is commonly observed during thrust faulting with strike-slip components (e.g. Dewey et al., 1998), as is supposed in our case.

During ongoing compressional deformation, the thrust fault tip progressively propagated upward and the shear zone gradually widened with the development of pervasive K1 fabric (Fig. 18a, b). The K1 fabric mainly developed at temperatures of 50-70°C, as indicated by clumped isotopes from veins associated with the K1 fabric (Fig. 15). Such temperatures differ from the values (150-200 °C) proposed by Bigi (2006), who studied the morphology of twin lamellae in calcite crystals. This remarkable difference may be explained by the still unclear relationship between the morphological aspect of twinning and temperature. Calcite twinning is indeed documented both in natural and experimental rocks deformed under a wide range of strain, temperature, and confining pressure (e.g. Rybacki et al., 2013; Mercuri et al., 2018; Demurtas et al., 2019). The paleofluid temperature of 50-70°C is consistent with thermal modelling estimates, which show that the sedimentary succession at the footwall of the MTT experienced maximum burial at temperature of about 70°C (Fig. 16).

The K1 fabric developed under repeated fluid overpressure and shear events as testified by: 1) the mutual cross-cutting relationships observed between calcite veins and dissolution planes (Fig. 8d and 18c); 2) and 2) the occurrence of partially dissolved and mechanically twinned calcite veins (Fig. 8c,d,e,f, 10b). Shear events are associated with pressure solution, as testified by the development of dissolution S planes, and frictional sliding. In particular, occurrence of frictional sliding is inferred by: 1) macroscopic slickenlines and slickenfibers observed along C, C', and (less frequently) S

planes; 2) microscopic sharp surfaces that bound calcite veins arranged along shear planes (Fig. 10b). Episodic fluid overpressure events are consistent with the occurrence of variously oriented sets of veins with crack-and-seal texture. In particular, each crack-and-seal event implies crack opening and precipitation of blocky crystals in fluid-filled open cracks (Bons, 2000; Hilgers and Urai, 2002; Hilgers et al., 2004; Bons et al., 2012). The alternating events of veining and shearing registered within the K1 fabric suggest multiple episodes of weakening (strain softening) and strengthening (strain hardening) through time during compressional orogenic deformation. In particular, weakening processes are related to fluid overpressure, which can reduce the effective stress acting on the shear zone (e.g. Bayerlee, 1990), and development of S-C/C' fabric (i.e. planar anisotropies) during shear events (e.g. Rutter, 1976). Strengthening processes are instead due to precipitation of calcite veins that are relatively stronger than the marly host rock (e.g. Kennedy and Logan, 1997; Torgersen and Viola, 2014). The observed homogeneous CL pattern of calcite veins testifies for the lack of significant fluid chemistry changes during these precipitation events (Fig. 9; Bons et al., 2012). Furthermore, the rather similar δ^{18}O and δ^{13}C values between calcite mineralizations of K1 fabric and host rocks suggest a long-term entrapment of mineralizing fluids within the host rock (i.e. fluids isotopically buffered by the host rock; e.g. Ghisetti et al., 2001; Agosta and Kirschner, 2003; Fig. 18a). On the contrary, the occurrence of sylvite microcrystals above the PSZ (Fig. S3d, S5c) suggests an upward migration along the thrust surface of fluids derived from Triassic evaporites (Fig. 18a), which form one of the main detachment level in the Central Apennines (e.g. Massoli et al., 2006; Cosentino et al., 2010). The presence of calcite veins parallel to the S planes (i.e. orthogonal to the maximum stress orientation; Fig. 8a,b,f) indicates that foliation acted as weakness surfaces, along which fractures developed during repeated fluid overpressure events, therefore providing high conductivity pathways for channelized fluid flow (e.g. Bruna et al., 2019). Furthermore, the occurrence of calcite veins bounding poorly foliated and rigid sigmoidal lithons (Fig. 8a,b) suggests a rotation of the sigmoidal lenses with development of calcite-filled dilational fractures during compressional deformation (Fig. 18c).

Up to ~40° clockwise rotation of the maximum shortening axis of the strain ellipsoid occurred during compressional orogenic stages, as indicated by the transition from transpressional (top-to-NE sense of shear) to reverse (top-to-E sense of shear) kinematics along the N-S striking, W dipping MTT. In detail, the top-to-NE kinematics is consistent with NE-verging folds with NW-SE-trending axis, whereas the younger top-to-E shear is testified both by kinematic indicators on the exposed thrust surface and by local slickenfibers associated with the K1 fabric. In the late stage of compressional deformation, when the MTT cut the entire sedimentary succession, two splays displaced the already developed footwall syncline (see geological sections in Figs. 2 and 18a, b).

As far as the deformation mechanisms are concerned, the MTT exhibits a combination of mainly distributed and, in places, localized deformation, which reflects the rheological contrast over the deformed lithotypes. In particular, the localized thrust surface (Fig. 6a), the competent lenses in proximity of the thrust surface (Fig. 6e), and the faulted rigid blocks within the shear zone (Fig. 4b, 18c) suggest high frictional strength and potentially unstable frictional (i.e. seismic) behaviour (e.g. Faulkner et al., 2003; Collettini et al., 2011). On the other hand, fault rocks that show ductile shear and foliation (such as S-C/C' tectonites developed by pressure-solution creep) are believed to be characterized by low frictional strength and, in the literature, are generally considered as the result of aseismic deformations (Rutter, 1976; Sibson, 1986; Gratier and Gamond, 1990; Gratier et al., 2011; Tesei et al., 2013; Fagereng and Hartog, 2016). In analogy with similar faults and fault rocks in the literature (Faulkner and Rutter, 2001; Faulkner et al, 2003, Collettini et al., 2011b, Tesei et al., 2013), we therefore suggest a general "mixed mode" mechanical behaviour for the MTT involving long-term alternation of earthquakes and aseismic events (multiple seismic cycles) during the compressional orogenic deformation.

6.4 Extensional evolution of the MTT

In the late Pliocene (IAA age of 2.88 Ma), the above described ~1700 m stack of thrust sheets was cut by NNE-SSW and NE-SW trending normal and oblique-normal faults and the MTT was partially extensionally-inverted (Fig. 18a,b). The MTT inversion (documented also by Bigi, 2006) is consistent with observed slickenfibers indicating normal fault slip motion along the fault surface (Fig. 6d) and produced also a K2 fabric that is diffuse within the first 10-15 metres below the thrust surface (Fig. 6b and see 3D block in Fig. S1). The shear zone bearing the K2 fabric developed at depths of ~800 m during exhumation (Fig. 18a). This is testified by the calculated paleofluid temperature of about 28°C (Fig. 15) in agreement with the estimated temperature experienced by the footwall succession at a depth of ~800 m during exhumation (Fig. 16). Furthermore, as testified by the decrease of δ^{18}O values from an average of 29 ‰ to 22.9‰ (Fig. 15), an opening of the fluid system with input of meteoric-derived fluids occurred during the extensional tectonic inversion of the MTT (Fig. 18a; Ghisetti et al., 2001; Agosta and Kirschner, 2003).

The K2 fabric developed under fluid pressure fluctuations associated with dissolution processes during shear events. In detail, the observed fibrous calcite veins within the K2 fabric (Fig. 11d, 18c) indicate the occurrence of small incremental growth of calcite crystals during shear events (e.g. Hilgers and Urai, 2005; Tesei et al., 2013) rather than distinct and repeated events of fluid overpressure and rapid growth of calcite veins. Microstructures from K2 fabric suggest that its development induced both folding and displacement of earlier K1 fabric, consistent with the

occurrence of partially preserved (folded and/or cut) S planes of K1 fabric within the well-developed K2 fabric (Fig. 11, 12, 18c). Similar characteristics are observed at the outcrop scale, where local folding and re-use of the earlier K1 fabric are recorded by relics of the K1 fabric preserved within the extensionally-inverted portion of the shear zone (Fig. 7, 18c), although no clear correlation between density of relics of K1 fabric and distance from the fault surface can be established.

Folding, displacement and/or overprinting of compressional structures can also be related to syn-late thrusting gravitational collapse (e.g. Tavani et al., 2011; Pace et al., 2016). Gravitational collapse is mainly accomodated by foreland-directed extensional structures (e.g. Butler et al., 1987; Pace et al., 2016) and, therefore, crosscutting relationship between syn-late thrusting extensional structures and post-compressive extensional structures may be observed (Pace et al., 2016). In the study area, no such crosscutting relationships and no foreland-directed structures are present. For these reasons, we suggest that the described extensional structures are ascribed to post-shortening extensional tectonics.

7. Conclusions

Based on our multidisciplinary approach, we draw a complex architecture and spatial-temporal evolution for the MTT. The orogenic and post-compressive evolution of the extensionally-inverted MTT can be summarized as follows:

1. Between ~9 and ~7 Ma, the orogenic deformation affected the Mt. Tancia area. The propagation of the MTT induced, at burial depths of ~1.5 km, the development and widening of the shear zone (K1 fabric). This fabric formed through repeated and alternating events of overpressure of fluids, which were long entrapped within the host rock, and shear events. The evolution of the whole structure of the MTT was essentially characterized by brittle-ductile deformation although different portions of the protolith experienced varying degrees of strain and strain localization attesting to the presence of rheology contrasts within the shear zone. In the late stage of compressional deformation, the footwall succession was deformed by two splays and reached a maximum burial depth of ~2 km.

2. At ~3 Ma, the MTT was affected by post-compressive extension and it was partially inverted. Tectonic inversion induced the development of the K2 fabric under fluid pressure fluctuation during shear events and with input of meteoric-derived fluids. The K2 fabric occurred at a maximum depth of ~800 m during exhumation. The tectonic inversion is recorded within the first metres below the thrust surface, in a zone dominated by partial tectonic superimposition, folding, displacement, and re-use of the earlier planar anisotropies of the compressional fabric.

The MTT represents an outstanding example of how: a) marly lithologies are prone to be deformed by brittle-ductile shear zones also under relatively low temperature (50-70°C); b) lithological contrasts can influence varying degrees of strain and strain localization within shear zones; c) pre-existing planar anisotropies (i.e. foliation planes) can represent weak discontinuities along which, during fluid overpressure events, tensional fractures can develop and mineral precipitation occur; d) the tectonic inversion may lead to a complex overprinting of early tectonic structures and fabrics by their (e.g. S-C/C' planes) partial re-use, displacement, and folding ; e) respect to an extensionally-inverted low-angle thrust, fluid circulation may be essentially host-rock- (subhorizontal flow) and meteoric-derived (subvertical flow) under compressional and extensional stress fields, respectively.

Aknowledgements

References

Agosta, F., & Kirschner, D. L. (2003). Fluid conduits in carbonate-hosted seismogenic normal faults of central Italy. Journal of Geophysical Research: Solid Earth, 108(B4).

Aldega, L., Botti, F., & Corrado, S. (2007). Clay mineral assemblages and vitrinite reflectance in the Laga Basin (Central Apennines, Italy): what do they record?. *Clays and Clay Minerals*, *55*(5), 504-518.

Aldega, L., Viola, G., Casas-Sainz, A., Marcén, M., Román-Berdiel, T. & van der Lelij, R. (2019). Unravelling multiple thermo-tectonic events accommodated by crustal-scale faults in northern Iberia, Spain: Insights from K-Ar dating of clay gouges. Tectonics doi: 10.1029/2019TC005585.

Allen, P. A., & Allen, J. R. (2013). Basin analysis: Principles and application to petroleum play assessment. John Wiley & Sons.

Bally, A. W. (1986). Balanced sections and seismic reflection profiles across the Central Apennines. *Mem. Soc. Geol. It.*, *35*, 257-310.

Balsamo, F., Aldega, L., De Paola, N., Faoro I., & Storti F. (2014). The signature and mechanics of earthquake ruptures along shallow creeping faults in poorly lithified sediments. *Geology, 42*, 435-438.

Bigi, S. (2006). An example of inversion in a brittle shear zone. *Journal of structural geology*, *28*(3), 431-443.

Billi, A., Tiberti, M. M., Cavinato, G. P., Cosentino, D., Di Luzio, E., Keller, J. V. A., Kluth, C., Orlando, L., Parotto, M., Praturlon, A., Romanelli, M., Storti, F., & Wardell, N. (2006). First results from the CROP-11 deep seismic profile, central Apennines, Italy: evidence of mid-crustal folding. Journal of the Geological Society, 163(4), 583-586.

Billi, A., & Tiberti, M. M. (2009). Possible causes of arc development in the Apennines, central Italy. *Geological Society of America Bulletin*, *121*(9-10), 1409-1420.

Blenkinsop, T. G., & Treloar, P. J. (1995). Geometry, classification and kinematics of SC and SC′ fabrics in the Mushandike area, Zimbabwe. *Journal of Structural Geology*, *17*(3), 397-408.

Bollati, A., Cipollari, P., Corrado, S., Cosentino, D., Danese, E., Marino, M., Mattei, M., & Parotto, M. (2009). New structural scheme of the Umbria-Sabina fold-and-thrust belt (Central Italy) derived from the geological mapping of 366 ''Palombara Sabina''and 375 ''Tivoli''sheets of the National Carg Project. Epitome, 3, 321.

Bons, P. D. (2000). The formation of veins and their microstructures. *Journal of the Virtual Explorer*, *2*, 12.

Bons, P. D., Elburg, M. A., & Gomez-Rivas, E. (2012). A review of the formation of tectonic veins and their microstructures. *Journal of Structural Geology*, *43*, 33-62.

Bruna, P. O., Lavenu, A. P., Matonti, C., & Bertotti, G. (2019). Are stylolites fluid-flow efficient features?. Journal of Structural Geology, 125, 270-277.

Burnham, A. K., & Sweeney, J.J. (1989). A chemical kinetic model of vitrinite maturation and reflectance. Geochimica et Cosmochimica Acta, 53(10), 2649-2657.

Butler, R. W., Coward, M. P., Harwood, G. M., & Knipe, R. J. (1987). Salt control on thrust geometry, structural style and gravitational collapse along the Himalayan mountain front in the Salt Range of northern Pakistan. In Dynamical geology of salt and related structures (pp. 339-418). Academic Press.

Byerlee, J. (1990). Friction, overpressure and fault normal compression. *Geophysical Research Letters*, *17*(12), 2109-2112.

Carminati, E., Lustrino, M., Cuffaro, M., & Doglioni, C. (2010). Tectonics, magmatism and geodynamics of Italy: what we know and what we imagine. *Journal of the Virtual Explorer*, *36*(8).

Caricchi C., Aldega L. & Corrado S. (2015a). Reconstruction of maximum burial along the Northern Apennines thrust wedge (Italy) by indicators of thermal exposure and modeling. Geological Society of American Bulletin, 127 (3-4), 428-442.

Caricchi C., Aldega L., Barchi, M., Corrado S., Grigo, D., Mirabella F. & Zattin M. (2015b). Exhumation patterns along shallow low-angle normal faults: an example from the Altotiberina active fault system (Northern Apennines, Italy). Terra Nova, 27 (4), 312-321.

Castellarin, A., Colacicchi, R., & Praturlon, A. (1978). *Fasi distensive, trascorrenze e sovrascorrimenti lungo la" Linea Ancona-Anzio", dal Lias medio al Pliocene*. Pinto.

Cavinato, G. P., & Celles, P. D. (1999). Extensional basins in the tectonically bimodal central Apennines fold-thrust belt, Italy: response to corner flow above a subducting slab in retrograde motion. *Geology*, *27*(10), 955-958.

Cavinato, G. P., Chiaretti, F., Cosentino, D., & Serva, L. (1989). Caratteri geologico-strutturali del margine orientale della Conca di Rieti. *Bollettino della Societa Geologica Italiana*, *108*(2), 207-218.

Cavinato, G. P., Salvini, F., & Tozzi, M. (1986). Evoluzione strutturale del settore centrale della linea Olevano-Antrodoco. *Memorie della Società Geologica Italiana*, *35*, 591-601.

Cipollari, P., Cosentino, D., & Parotto, M. (1997). Modello cinematicostrutturale dell'Italia centrale. *Studi Geologici Camerti*, *2*(135143).

Civitelli, G., Corda, L., & Mariotti, G. (1986a). Il bacino sabino: 2) sedimentologia e stratigrafia della serie calcarea e marnoso spongolitica (Paleogene-Miocene). *Memorie della Società Geologica Italiana*, *35*, 33-47.

Civitelli, G., Corda, L., & Mariotti, G. (1986b). Il bacino sabino: 3) evoluzione sedimentaria ed inquadramento regionale dall'Oligocene al Serravalliano. *Memorie della Società Geologica Italiana*, *35*(1), 399-406.

Clauer, N. (2013). The K-Ar and 40Ar/39Ar methods revisited for dating fine-grained K-bearing clay minerals. *Chemical Geology*, *354*, 163-185.

Collettini, C. (2011). The mechanical paradox of low-angle normal faults: Current understanding and open questions. *Tectonophysics*, *510*(3-4), 253-268.

Collettini, C., Niemeijer, A., Viti, C., & Marone, C. (2009). Fault zone fabric and fault weakness. *Nature*, *462*(7275), 907.

Collettini, C., Niemeijer, A., Viti, C., Smith, S. A., & Marone, C. (2011b). Fault structure, frictional properties and mixed-mode fault slip behavior. *Earth and Planetary Science Letters*, *311*(3-4), 316-327.

Collettini, C., Tesei, T., Scuderi, M. M., Carpenter, B. M., & Viti, C. (2019). Beyond Byerlee friction, weak faults and implications for slip behavior. *Earth and Planetary Science Letters*, *519*, 245-263.

Corda, L., & Mariotti, G. (1986). Il bacino Sabino; 1, Fenomeni di risedimentazione nella serie di Osteria Tancia. *Bollettino della Societa Geologica Italiana*, *105*(1-2), 41-63.

Corrado, S. (1995a). Nuovi vincoli geometrico-cinematici all'evoluzione neogenica del tratto meridionale della linea Olevano-Antrodoco. Bollettino della Società Geologica Italiana, 114(1), 245-276.

Corrado, S. (1995b). Optical parameters of maturity of organic matter dispersed in sediments: first results from the Central Apennines (Italy). Terra nova, 7(3), 338-347.

Corrado, S. (1996). Evoluzione termica e carico tettonico di alcune successioni sedimentarie dell'Appennino centrale: un esempio nelle aree di piattaforma carbonatica e di scarpata. Mem. Soc. Geol. Ital, 51, 527-541.

Corrado, S., Aldega, L., & Zattin, M. (2010). Sedimentary vs. tectonic burial and exhumation along the Apennines (Italy). *Journal of Virtual Explorer*, *36*.

Cosentino, D., & Parotto, M. (1986). Assetto strutturale dei Monti Lucretili settentrionali (Sabina): nuovi dati e schema tettonico preliminare. *Geologica Romana*, *25*, 73-90.

Cosentino, D., & Parotto, M. (1992). La struttura a falde della Sabina (Appennino centrale). *Studi geologici camerti*, n. speciale, pp. 381-387.

Cosentino, D., Cipollari, P., Marsili, P., & Scrocca, D. (2010). Geology of the central Apennines: a regional review. *Journal of the virtual explorer*, *36*(11), 1-37.

Cosentino, D., Miccadei, E., & Parotto, M. (1993). Assetto geologico-strutturale dei Monti di Fara in Sabina (Lazio, Appennino centrale). *Geologica Romana*, *29*, 537-545.

Cosentino, D., Miccadei, E., Barberi, R., Basilici, G., Cipollari, P., Parotto, M., & Piacentini, T. (2014). Note illustrative della Carta Geologica d'Italia alla scala 1: 50.000, Foglio 357-Cittaducale. *ISPRA-Servizio Geologico d'Italia*.

D'Agostino, N., Chamot-Rooke, N., Funiciello, R., Jolivet, L., & Speranza, F. (1998). The role of pre-existing thrust faults and topography on the styles of extension in the Gran Sasso range (central Italy). Tectonophysics, 292(3-4), 229-254.

Davis, G. H., Reynolds, S. J., & Kluth, C. F. (2011). *Structural geology of rocks and regions*. John Wiley & Sons.

Della Vedova, B., Mongelli, F., Pellis, G., Squarci, P., Taffi, L., & Zito, G. (1991). Heat flow map of Italy.

Dewey, J. F., Holdsworth, R. E., & Strachan, R. A. (1998). Transpression and transtension zones. *Geological Society, London, Special Publications*, *135*(1), 1-14.

Demurtas, M., Smith, S. A., Prior, D. J., Spagnuolo, E., & Di Toro, G. (2019). Development of crystallographic preferred orientation during cataclasis in low-temperature carbonate fault gouge. Journal of Structural Geology, 126, 37-50.

Doglioni, C., Moretti, I., & Roure, F. (1991). Basal lithospheric detachment, eastward mantle flow and Mediterranean geodynamics: a discussion. *Journal of Geodynamics*, *13*(1), 47-65.

Faccenna, C., Nalpas, T., Brun, J. P., Davy, P., & Bosi, V. (1995). The influence of pre-existing thrust faults on normal fault geometry in nature and in experiments. *Journal of Structural Geology*, *17*(8), 1139-1149.

Fagereng, Å., & Den Hartog, S. A. (2017). Subduction megathrust creep governed by pressure solution and frictional–viscous flow. *Nature Geoscience*, *10*(1), 51.

Faulkner, D. R., Lewis, A. C., & Rutter, E. H. (2003). On the internal structure and mechanics of large strike-slip fault zones: field observations of the Carboneras fault in southeastern Spain. *Tectonophysics*, *367*(3-4), 235-251.

Faulkner, D. R., & Rutter, E. H. (2001). Can the maintenance of overpressured fluids in large strike-slip fault zones explain their apparent weakness?. Geology, 29(6), 503-506.

Gratier, J. P., & Gamond, J. F. (1990). Transition between seismic and aseismic deformation in the upper crust. *Geological Society, London, Special Publications*, *54*(1), 461-473.

Gratier, J. P., Richard, J., Renard, F., Mittempergher, S., Doan, M. L., Di Toro, G., Hadizadeh, J. & Boullier, A. M. (2011). Aseismic sliding of active faults by pressure solution creep: Evidence from the San Andreas Fault Observatory at Depth. *Geology*, *39*(12), 1131-1134.

Hilgers, C., & Urai, J. L. (2002). Microstructural observations on natural syntectonic fibrous veins: implications for the growth process. *Tectonophysics*, *352*(3-4), 257-274.

Hilgers, C., & Urai, J. L. (2005). On the arrangement of solid inclusions in fibrous veins and the role of the crack-seal mechanism. *Journal of Structural Geology*, *27*(3), 481-494.

Hilgers, C., Dilg-Gruschinski, K., & Urai, J. L. (2004). Microstructural evolution of syntaxial veins formed by advective flow. *Geology*, *32*(3), 261-264.

Hillier, S., Matyas, J., Matter, A., & Vasseur, G. (1995). Illite/smectite diagenesis and its variable correlation with vitrinite reflectance in the Pannonian Basin. Clays and Clay Minerals, 43(2), 174-183.

Holdsworth, R. E., Butler, C. A., & Roberts, A. M. (1997). The recognition of reactivation during continental deformation. *Journal of the Geological Society*, *154*(1), 73-78.

Holdsworth, R. E., Stewart, M., Imber, J., & Strachan, R. A. (2001). The structure and rheological evolution of reactivated continental fault zones: a review and case study. *Geological Society, London, Special Publications*, *184*(1), 115-137.

ISPRA (APAT) – Servizio Geologico d'Italia, Carta Geologica d'Italia alla scala 1:50.000-Foglio n. 357 "Cittaducale".

Ivins, E. R., Dixon, T. H., & Golombek, M. P. (1990). Extensional reactivation of an abandoned thrust: a bound on shallowing in the brittle regime. *Journal of Structural Geology*, *12*(3), 303-314.

Kennedy, L. A., & Logan, J. M. (1997). The role of veining and dissolution in the evolution of fine-grained mylonites: the McConnell thrust, Alberta. *Journal of Structural Geology*, *19*(6), 785-797.

Kralik, M., Klima, K., & Riedmüller, G. (1987). Dating fault gouges. *Nature*, *327*(6120), 315.

Lucca, A., Storti, F., Balsamo, F., Clemenzi, L., Fondriest, M., Burgess, R., & Di Toro, G. (2019). From Submarine to Subaerial Out-of-Sequence Thrusting and Gravity-Driven Extensional Faulting: Gran Sasso Massif, Central Apennines, Italy. Tectonics.

Lyons, J. B., & Snellenburg, J. (1971). Dating faults. *Geological Society of America Bulletin*, *82*(6), 1749-1752.

Malavieille, J. (1987). Kinematics of compressional and extensional ductile shearing deformation in a metamorphic core complex of the northeastern Basin and Range. *Journal of Structural Geology*, *9*(5-6), 541-554.

Malinverno, A., & Ryan, W. B. (1986). Extension in the Tyrrhenian Sea and shortening in the Apennines as result of arc migration driven by sinking of the lithosphere. *Tectonics*, *5*(2), 227-245.

Marchesini, B., Garofalo, P. S., Menegon, L., Mattila, J., & Viola, G. (2019). Fluid-mediated, brittle–ductile deformation at seismogenic depth–Part 1: Fluid record and deformation history of fault veins in a nuclear waste repository (Olkiluoto Island, Finland). Solid Earth, 10(3), 809-838.

Massoli, D., Koyi, H. A., & Barchi, M. R. (2006). Structural evolution of a fold and thrust belt generated by multiple décollements: analogue models and natural examples from the Northern Apennines (Italy). *Journal of Structural Geology*, *28*(2), 185-199.

Mazzoli, S., Pierantoni, P. P., Borraccini, F., Paltrinieri, W., & Deiana, G. (2005). Geometry, segmentation pattern and displacement variations along a major Apennine thrust zone, central Italy. Journal of Structural Geology, 27(11), 1940-1953.

Mercuri, M., Scuderi, M. M., Tesei, T., Carminati, E., & Collettini, C. (2018). Strength evolution of simulated carbonate-bearing faults: The role of normal stress and slip velocity. Journal of Structural Geology, 109, 1-9.

Merriman, R. J., & Frey, M. (1998). Patterns of very low-grade metamorphism in metapelitic rocks. *Low-grade metamorphism*, 61-107.

Migliorini, C. I. (1948). I cunei composti nell'orogenesi. Bollettino della Società Geologica Italiana, 67 (1948), pp. 29-142.

Moore, D. E., & Rymer, M. J. (2007). Talc-bearing serpentinite and the creeping section of the San Andreas fault. *Nature*, *448*(7155), 795.

Pace, P., Pasqui, V., Tavarnelli, E., & Calamita, F. (2016). Foreland-directed gravitational collapse along curved thrust fronts: insights from a minor thrust-related shear zone in the Umbria–Marche belt, central-northern Italy. Geological Magazine, 154(2), 381-392.

Passchier, C. W. (1987). Stable positions of rigid objects in non-coaxial flow—a study in vorticity analysis. *Journal of Structural Geology*, *9*(5-6), 679-690.

Passchier, C. W. (1991). The classification of dilatant flow types. *Journal of Structural Geology*, *13*(1), 101-104.

Pevear, D. R. (1999). Illite and hydrocarbon exploration. *Proceedings of the National Academy of Sciences*, *96*(7), 3440-3446.

Ring, U., & Gerdes, A. (2016). Kinematics of the Alpenrhein-Bodensee graben system in the Central Alps: Oligocene/Miocene transtension due to formation of the Western Alps arc. *Tectonics*, *35*(6), 1367-1391.

Rutter, E. H. (1976). A discussion on natural strain and geological structure-the kinetics of rock deformation by pressure solution. *Philosophical Transactions of the Royal Society of London. Series A, Mathematical and Physical Sciences*, *283*(1312), 203-219.

Rutter, E. H., Maddock, R. H., Hall, S. H., & White, S. H. (1986). Comparative microstructures of natural and experimentally produced clay-bearing fault gouges. *Pure and Applied Geophysics*, *124*(1-2), 3-30.

Rybacki, E., Evans, B., Janssen, C., Wirth, R., & Dresen, G. (2013). Influence of stress, temperature, and strain on calcite twins constrained by deformation experiments. Tectonophysics, 601, 20-36.

Scheiber, T., & Viola, G. (2018). Complex bedrock fracture patterns: A multipronged approach to resolve their evolution in space and time. *Tectonics*, *37*(4), 1030-1062.

Sclater, J. G., & Christie, P. A. (1980). Continental stretching: An explanation of the post-Mid-Cretaceous subsidence of the central North Sea Basin. Journal of Geophysical Research, 85(B7), 3711‑3739.

Środoń, J. (1999). Nature of mixed-layer clays and mechanisms of their formation and alteration. Annual Review of Earth and Planetary Sciences, 27(1), 19-53.

Sibson, R. H. (1986). Brecciation processes in fault zones: inferences from earthquake rupturing. *Pure and Applied Geophysics*, *124*(1-2), 159-175.

Sibson, R. H. (1990). Conditions for fault-valve behaviour. *Geological Society, London, Special Publications*, *54*(1), 15-28.

Sibson, R. H. (1995). Selective fault reactivation during basin inversion: potential for fluid redistribution through fault-valve action. *Geological Society, London, Special Publications*, *88*(1), 3-19.

Sibson, R. H. (2000). Fluid involvement in normal faulting. *Journal of Geodynamics*, *29*(3-5), 469-499.

Sweeney, J.J., & Burnham, A.K. (1990). Evaluation of a simple model of vitrinite reflectance based on chemical kinetics (1). *American Association of Petroleum Geologists Bulletin*, *74*(10), 1559-1570.

Smeraglia, L., Billi, A., Carminati, E., Cavallo, A., Di Toro, G., Spagnuolo, E., & Zorzi, F. (2017). Ultra-thin clay layers facilitate seismic slip in carbonate faults. Scientific reports, 7(1), 664.

Smith, S. A. F., Tesei, T., Scott, J. M., & Collettini, C. (2017). Reactivation of normal faults as high-angle reverse faults due to low frictional strength: Experimental data from the Moonlight Fault Zone, New Zealand. *Journal of Structural Geology*, *105*, 34-43.

Smith, S. A., Billi, A., Di Toro, G., & Spiess, R. (2011). Principal slip zones in limestone: microstructural characterization and implications for the seismic cycle (Tre Monti Fault, Central Apennines, Italy). *Pure and Applied Geophysics*, *168*(12), 2365-2393.

Środoń, J., 1999. Nature of mixed-layer clays and mechanisms of their formation and alteration: *Annual Review of Earth and Planetary Sciences, 27*, 19-53.

Suppe, J., & Medwedeff, D. A. (1990). Geometry and kinematics of fault-propagation folding. *Eclogae Geologicae Helvetiae*, *83*(3), 409-454.

Tavani, S., Vignaroli, G., & Parente, M. (2015). Transverse versus longitudinal extension in the foredeep-peripheral bulge system: Role of Cretaceous structural inheritances during early Miocene extensional faulting in inner central Apennines belt. Tectonics, 34(7), 1412-1430.

Tavani, S., Mencos, J., Bausà, J., & Muñoz, J. A. (2011). The fracture pattern of the Sant Corneli Bóixols oblique inversion anticline (Spanish Pyrenees). Journal of Structural Geology, 33(11), 1662-1680.

Tesei, T., Collettini, C., Barchi, M. R., Carpenter, B. M., & Di Stefano, G. (2014). Heterogeneous strength and fault zone complexity of carbonate-bearing thrusts with possible implications for seismicity. *Earth and Planetary Science Letters*, *408*, 307-318.

Tesei, T., Collettini, C., Viti, C., & Barchi, M. R. (2013). Fault architecture and deformation mechanisms in exhumed analogues of seismogenic carbonate-bearing thrusts. *Journal of Structural Geology*, *55*, 167-181.

Torgersen, E., & Viola, G. (2014). Structural and temporal evolution of a reactivated brittle–ductile fault–Part I: Fault architecture, strain localization mechanisms and deformation history. *Earth and Planetary Science Letters*, *407*, 205-220.

Torgersen, E., Viola, G., Zwingmann, H., & Harris, C. (2015a). Structural and temporal evolution of a reactivated brittle–ductile fault–Part II: Timing of fault initiation and reactivation by K–Ar dating of synkinematic illite/muscovite. *Earth and Planetary Science Letters*, *410*, 212-224.

Torgersen, E., Viola, G., Zwingmann, H., & Henderson, I. H. (2015b). Inclined K–Ar illite age spectra in brittle fault gouges: effects of fault reactivation and wall-rock contamination. *Terra Nova*, *27*(2), 106-113.

Uysal, I. T., Mutlu, H., Altunel, E., Karabacak, V., & Golding, S. D. (2006). Clay mineralogical and isotopic (K–Ar, δ18O, δD) constraints on the evolution of the North Anatolian Fault Zone, Turkey. *Earth and Planetary Science Letters*, *243*(1-2), 181-194.

Vignaroli, G., Aldega, L., Balsamo, F., Billi, A., De Benedetti, A.A., De Filippis, L., Giordano, G. & Rossetti, F. (2015). A way to hydrothermal paroxysm, Colli Albani Volcano, Italy. *Geological Society of American Bulletin, 127* (5-6), 672-687.

Vignaroli, G., Berardi, G., Billi, A., Kele, S., Rossetti, F., Soligo, M., & Bernasconi, S. M. (2016). Tectonics, hydrothermalism, and paleoclimate recorded by Quaternary travertines and their spatio-temporal distribution in the Albegna basin, central Italy: Insights on Tyrrhenian margin neotectonics. *Lithosphere*, *8*(4), 335-358.

Viola, G., Scheiber, T., Fredin, O., Zwingmann, H., Margreth, A., & Knies, J. (2016). Deconvoluting complex structural histories archived in brittle fault zones. *Nature communications*, *7*, 13448.

Viola, G., Torgersen, E., Mazzarini, F., Musumeci, G., van der Lelij, R., Schönenberger, J., & Garofalo, P. S. (2018). New Constraints on the Evolution of the Inner Northern Apennines by K-Ar Dating of Late Miocene-Early Pliocene Compression on the Island of Elba, Italy. *Tectonics*, *37*(9), 3229-3243.

Viola, G., Zwingmann, H., Mattila, J., & Käpyaho, A. (2013). K-Ar illite age constraints on the Proterozoic formation and reactivation history of a brittle fault in Fennoscandia. *Terra Nova*, *25*(3), 236-244.

Vrolijk, P., & van der Pluijm, B. A. (1999). Clay gouge. *Journal of structural Geology*, *21*(8-9), 1039-1048.

Williams, G. D., Powell, C. M., & Cooper, M. A. (1989). Geometry and kinematics of inversion tectonics. *Geological Society, London, Special Publications*, *44*(1), 3-15.

Zwingmann, H., Offler, R., Wilson, T., & Cox, S. F. (2004). K–Ar dating of fault gouge in the northern Sydney Basin, NSW, Australia—implications for the breakup of Gondwana. *Journal of Structural Geology*, *26*(12), 2285-2295.
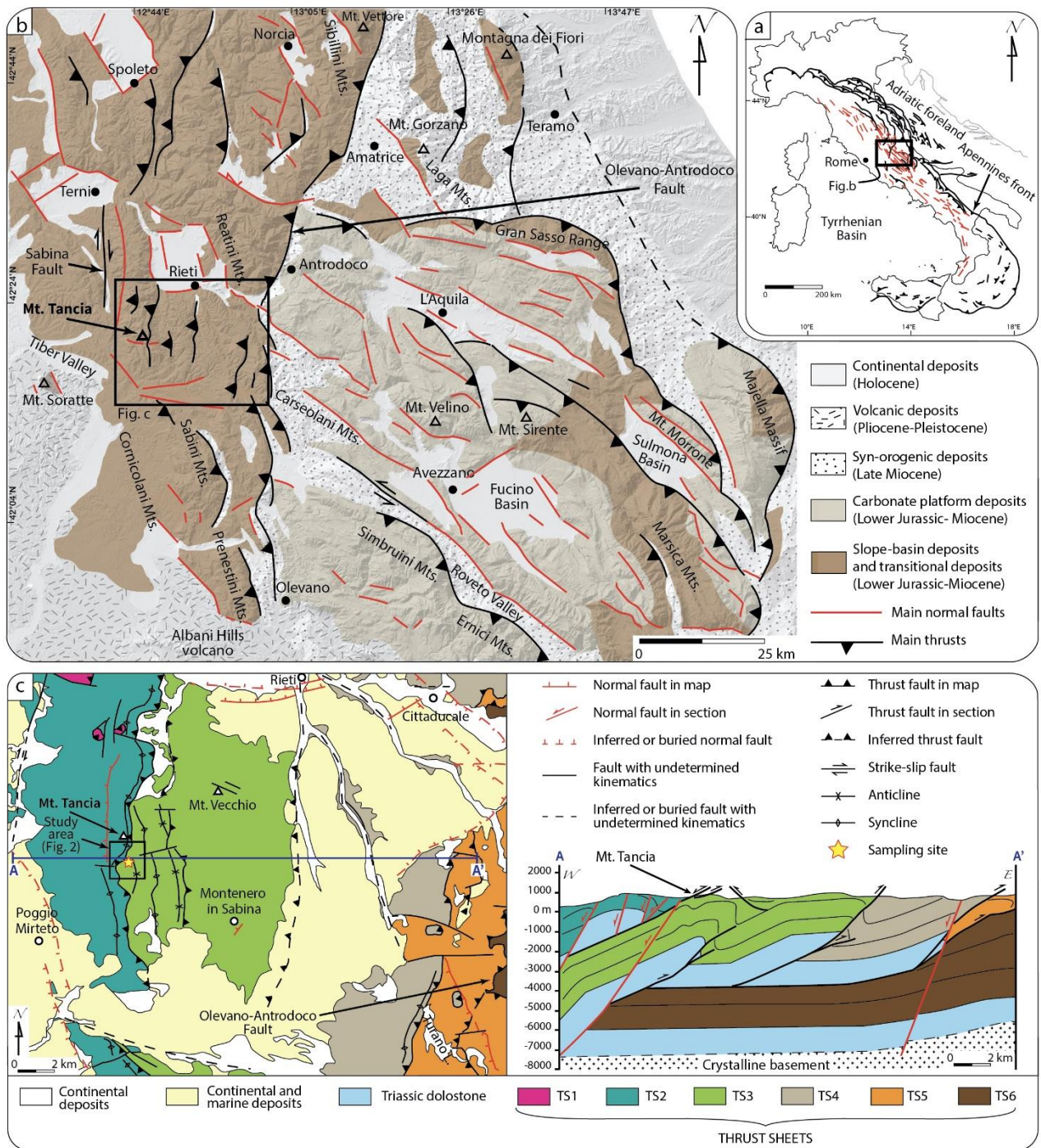
Figure 1. (a) Simplified structural map of Italy with main extensional faults in red and main thrust-reverse faults in black. (b) Simplified geological map of the central-northern Apennines, showing main thrusts and extensional faults as well as the location of the study area (i.e. Mt. Tancia). (c) Tectonic scheme and geological cross section of the central portion of Sabine thrust belt including the Mt. Tancia Thrust (MTT) that is studied in this paper (modified and redrawn after Cosentino et al., 2014). The yellow star shows the sampling site for calcite mineralizations, host rocks, and fault gouge. See Fig. 2 for detailed location of sampling sites.
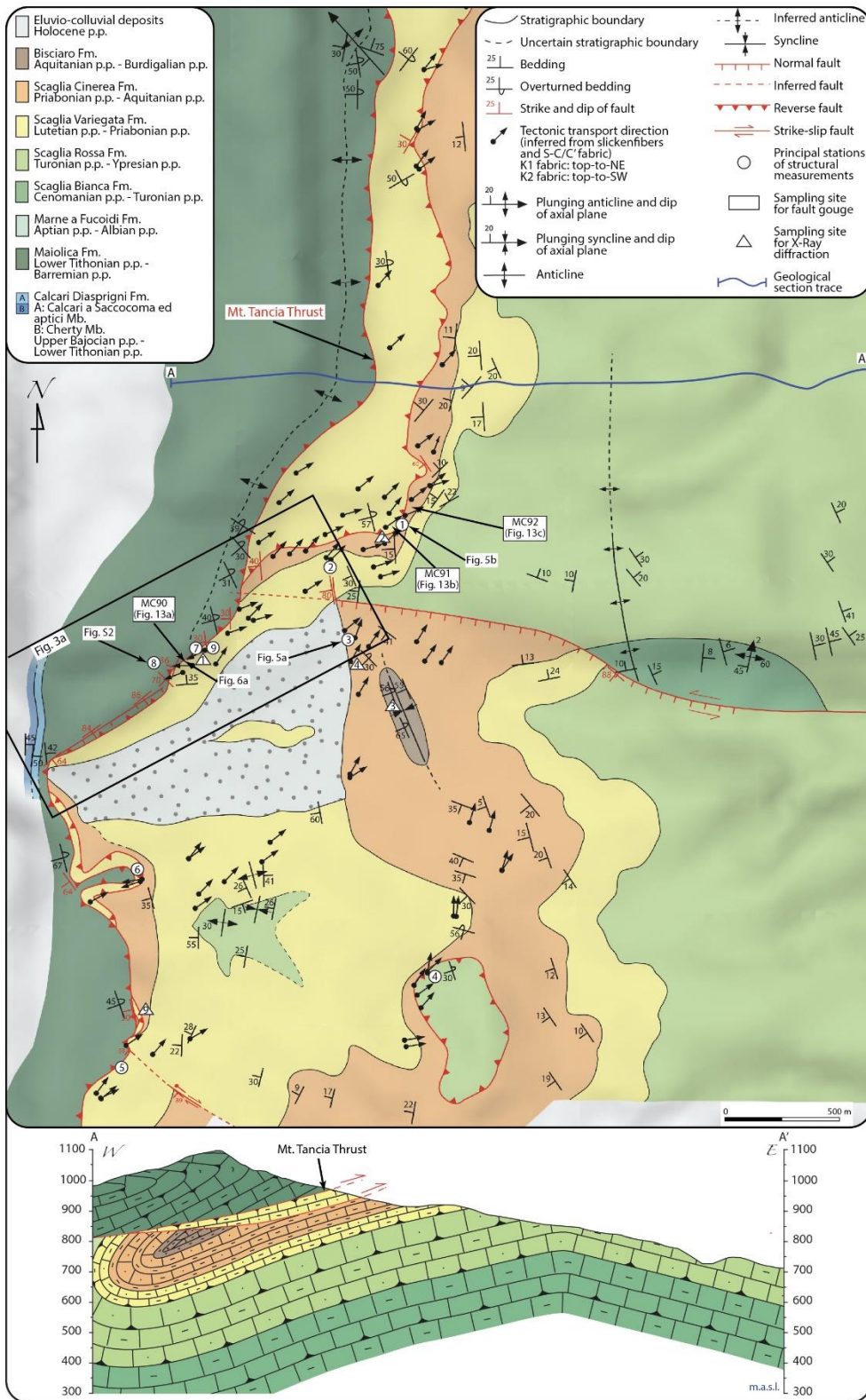
Figure 2. Simplified geological-structural map and geological cross section of the Mt. Tancia Thrust. Sampling location for K-Ar dating, structural and X-ray diffraction analysis is shown. A more detailed geological-structural map is available in the supplementary material (Fig. S2).
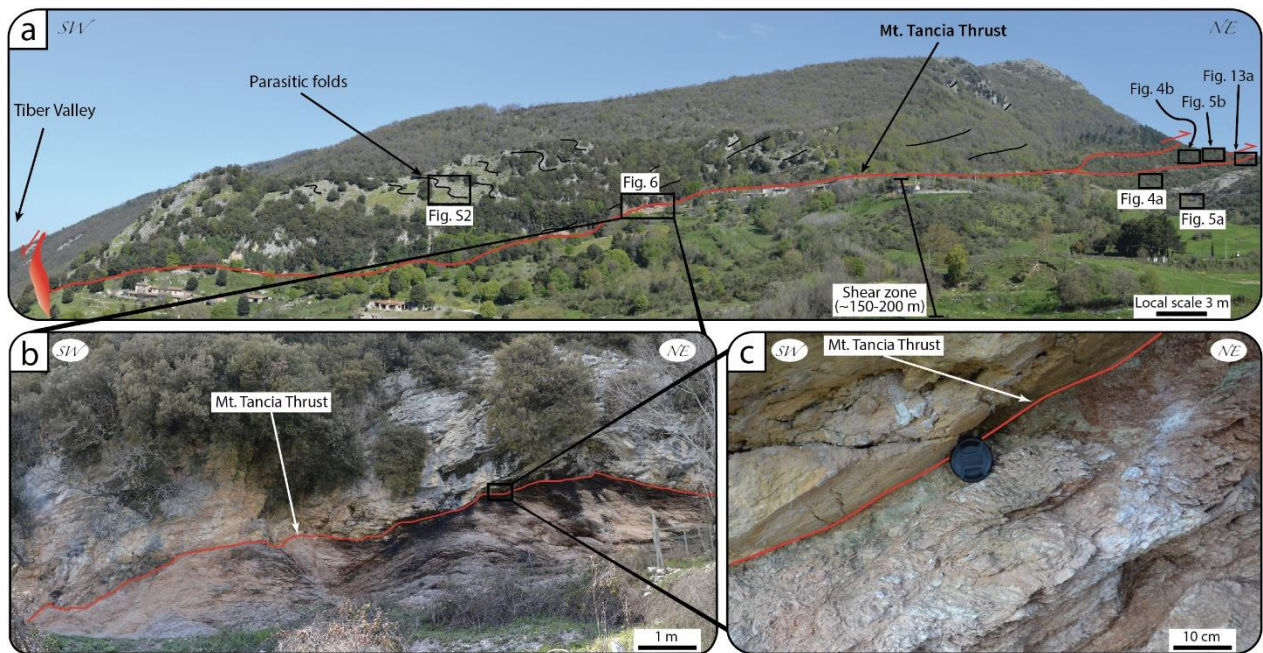
Figure 3. (a) Panoramic view of the southern flank of the Mt. Tancia (see Fig. 2 for location) with geological interpretation and location of some studied outcrops. (b) The best known exposure of MTT (structural site 7 in Fig. 2). (c) Detail of MTT. Line drawing and interpretation of (b) and (c) are shown in figure 6.
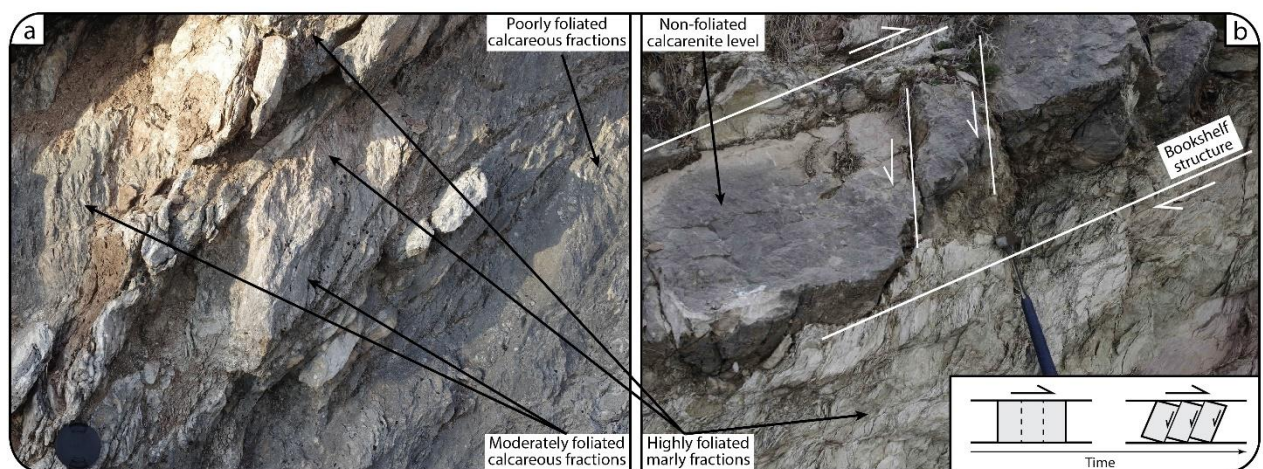
Figure 4. Outcrops of the Scaglia Variegata Fm. at the footwall of the MTT showing the close relationship between lithology and deformation (see Fig. 3a for locations). (a) The marly fractions are highly foliated with closely-spaced dissolution S planes. The more calcareous portions are moderately or weakly foliated, with widely spaced shear and dissolution planes. (b) The rigid calcarenite blocks are non-foliated and arranged in a bookshelf structure indicating dextral sense of shear, coherent with S-C fabric. Inset in (b) shows a schematic representation of the model for the development of a bookshelf structure by rotation of fault-bounded blocks within a zone of progressive simple shear.
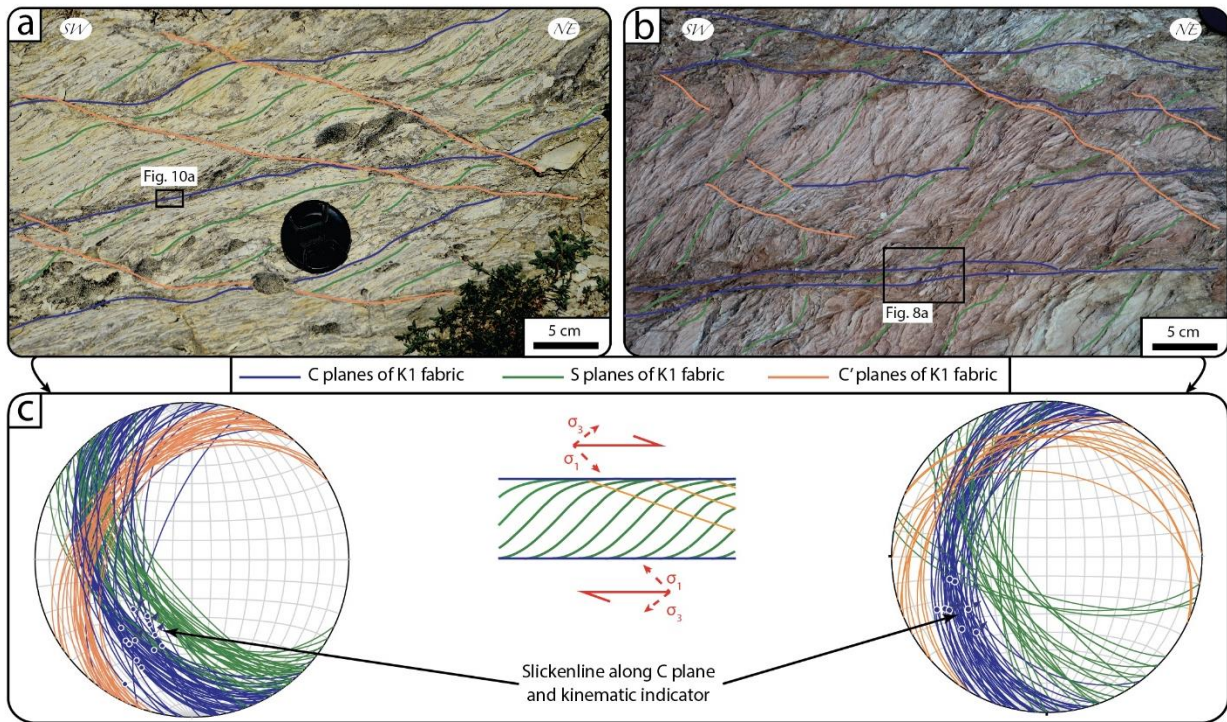
Figure 5. (a) S-C/C' fabric with a top-to-NE sense of shear developed in the Scaglia Cinerea Fm. (MTT footwall) and (b) in the Scaglia Variegata Fm. (MTT footwall) (see Figs. 2 and 3a for locations). (c) Schmidt nets (lower hemisphere projection) showing attitudes of S-C/C' fabric and related kinematic indicators (calcite slickenfibers).
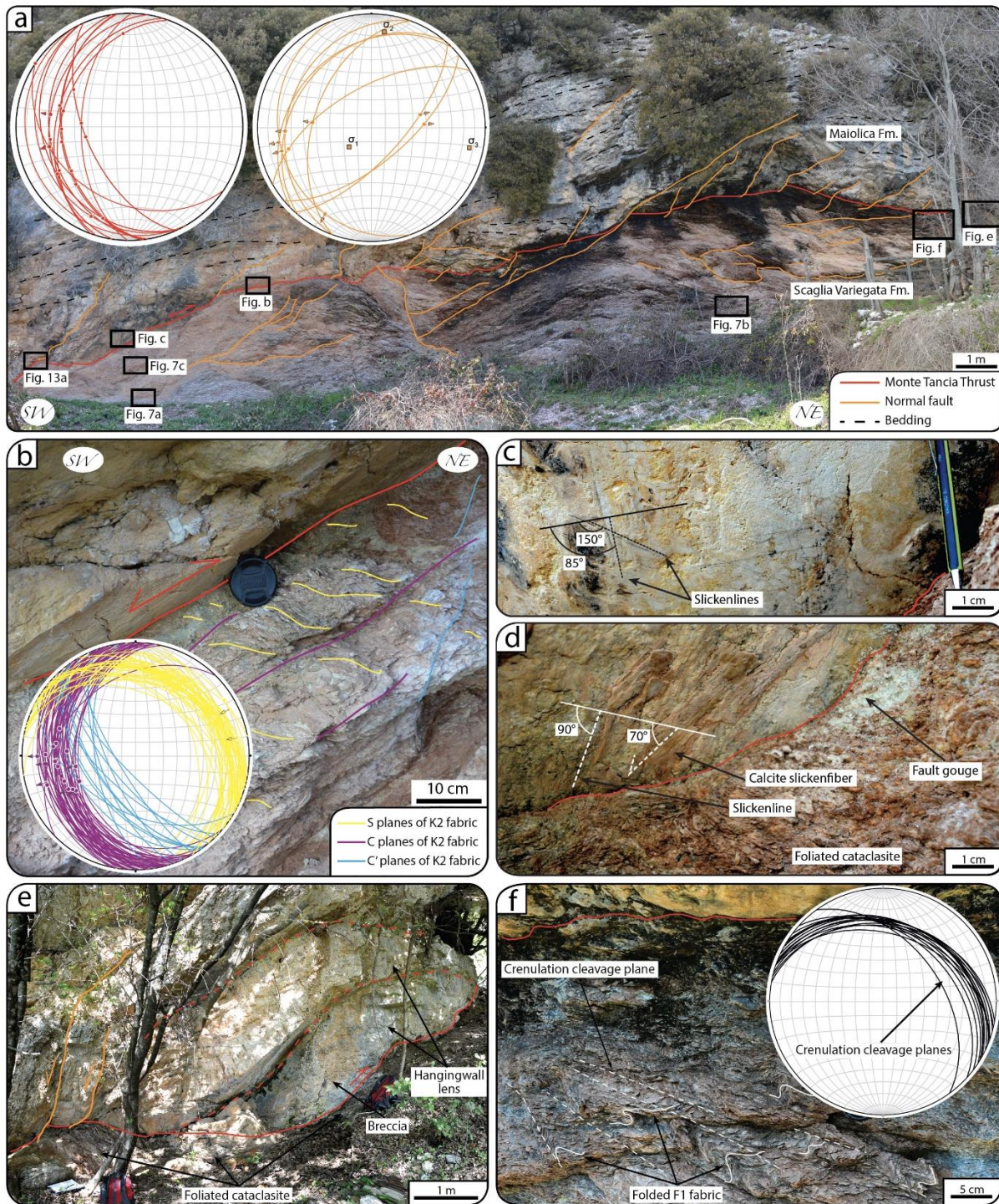
Figure 6. (a) The best known exposure of MTT with well-bedded Maiolica Fm. (at the hangingwall) above the highly foliated Scaglia Variegata Fm. (at the footwall; see Fig. 3a for location). The thrust surface is displaced by several high-angle and low-angle normal faults. Schmidt nets (lower hemisphere projection) show attitude of thrust fault and normal faults with related kinematic indicators. (b) Pervasive S-C/C' fabric (K1 fabric; top-to-W-SW) in the MTT footwall. Schmidt net (lower hemisphere projection) shows attitude of S-C/C' fabric and related kinematic indicators. (c, d) Slickenlines and calcite slickenfibers on the MTT surface. (e) Lenses of Maiolica Fm. at the MTT hangingwall forming a metric-scale imbricate structure. (f) Crenulation cleavage formed by centimetre-scale folding of K1 fabric. Schmidt net (lower hemisphere projection) shows attitude of K1 fabric. Notice the compatibility with the negative inversion of the MTT with a top-to-SW sense of shear.
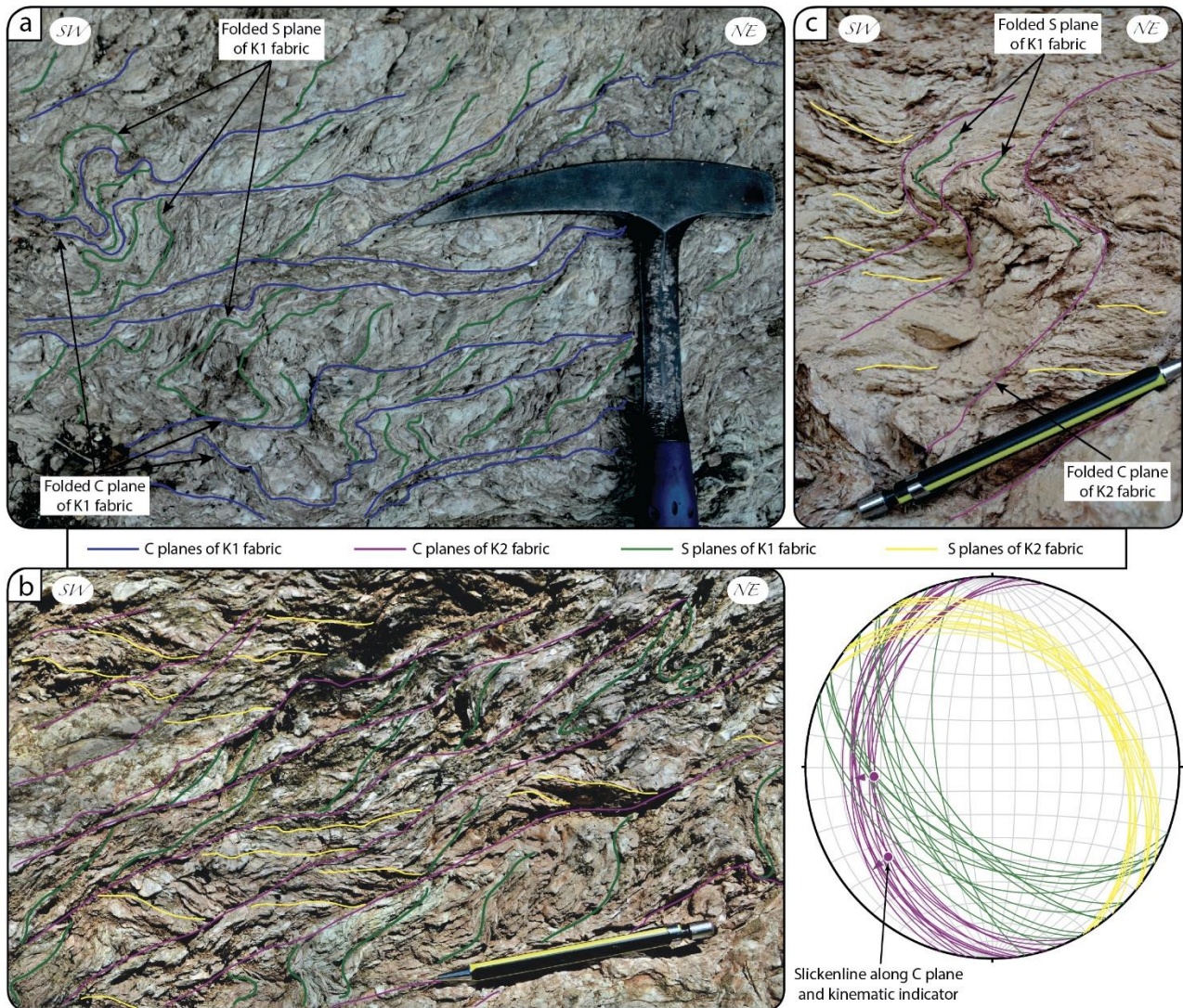
Figure 7. (a, b, c) Folded C and S planes of K1 fabric at the MTT footwall (see Fig. 6a for detailed location). Schmidt net (lower hemisphere projection) shows attitude of tectonic fabric. Notice the folded K1 fabric, which preserve the reverse sense of shear in (a). Notice the difference between the folded S planes of K1 fabric and the unfolded S planes of K2 fabric in (c). This difference suggests that, in places, during the tectonic inversion of the MTT, the C planes of K1 fabric (formed during the compressional phase) were initially folded and subsequently reused as shear planes with extensional kinematics.
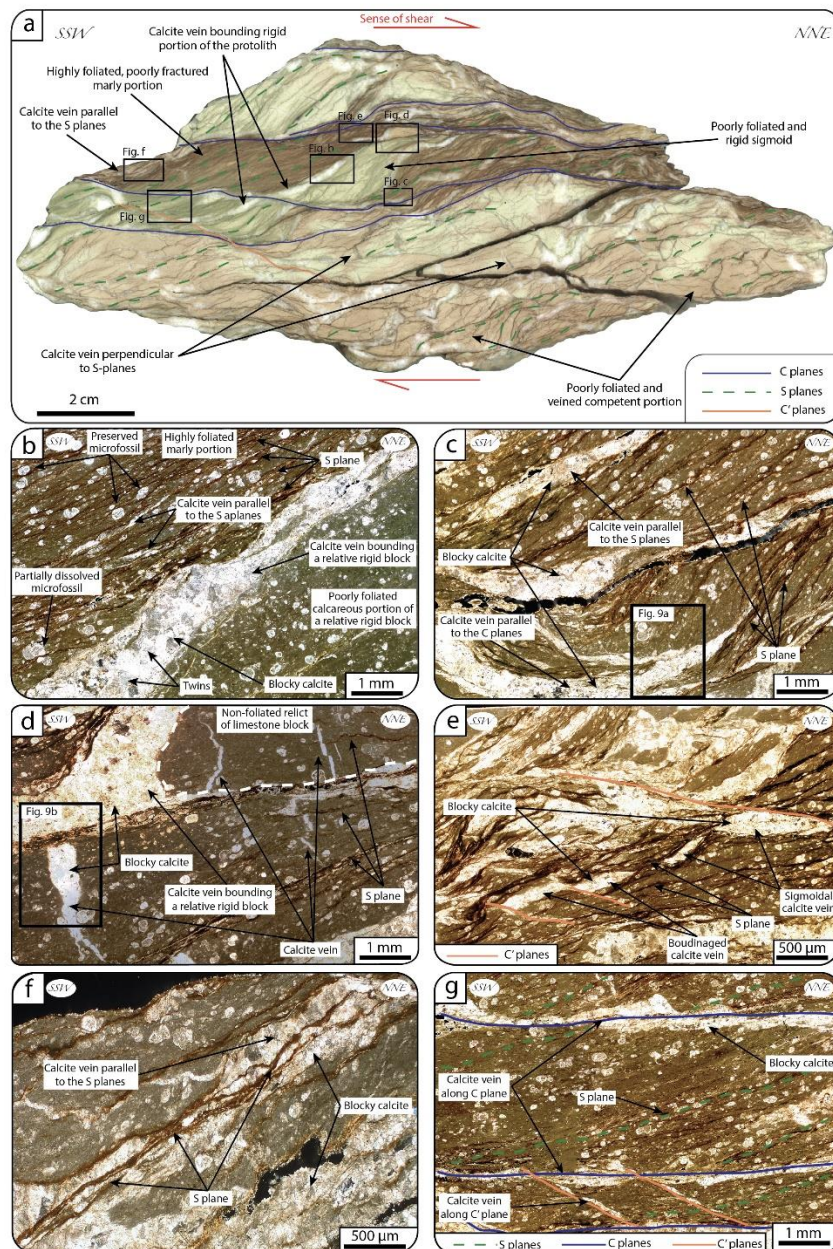
Figure 8. (a) High-resolution scan of S-C/C' K1 fabric developed in the marly limestones of the Scaglia Variegata Fm (see Fig. 5b). Notice the presence of microdomains with different styles of deformation. The more competent portions are poorly foliated and characterized by abundant and thick calcite veins. Sigmoidal blocks are packed into the highly foliated marly layers of the tectonites and are arranged consistently with the sense of shear. (b) Twinned calcite vein bounding rigid sigmoids. Notice the closely spaced dissolution planes in the marly fraction. Microfossils are preserved or only partially reworked. (c) Calcite vein parallel to the S planes and calcite vein parallel to the C planes, which are hooked upward into the dissolution planes. (d) Crosscutting relationship between calcite veins with respect to the dissolution planes. Notice the minor internal deformation of the non-foliated limestone block, which is bounded by twinned calcite crystals. (e) Detail of boudinaged and sigmoidal calcite vein arranged parallel to the S planes. (f) Calcite vein parallel to the S planes that are reworked by dissolution planes. (g) S-C/C' fabric at the microscale. Mineralizations along C planes are composed of blocky calcite veins bounded by scabrous (or teeth-

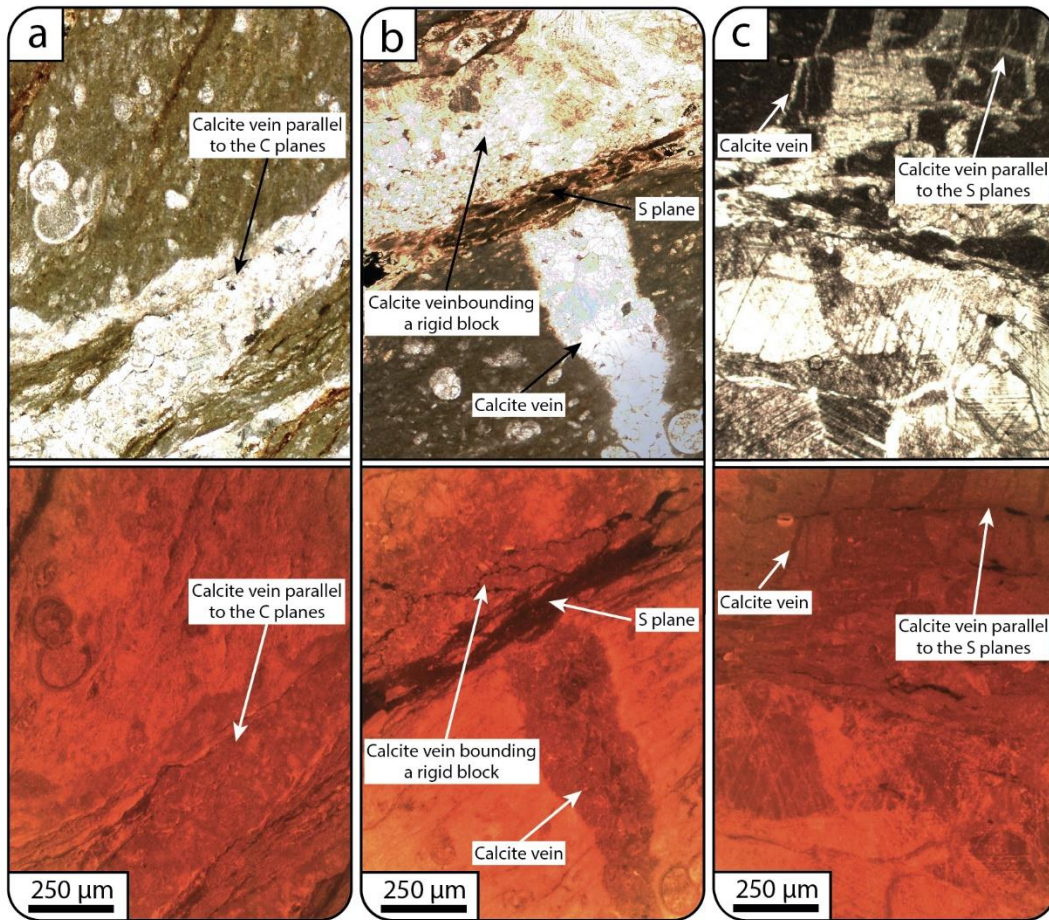shaped)   dissolution   planes.

Figure 9. Microphotograph and corresponding observation under cathodoluminescence light of the different sets of calcite veins within the K1 fabric. The cements in the fractures are very similar, dull in cathodoluminescence, although some minor differences can be observed. No zonation is present, suggesting precipitation from homogeneous fluids (a) Calcite veins parallel to the C planes (see Fig. 8c). (b) Variously oriented calcite veins bounding a relative rigid block (see Fig. 8d). (c) Variously oriented calcite veins parallel to the S planes; notice the fractured veins in the upper part and the image, slightly darker than the blocky cements in the lower part of the image.
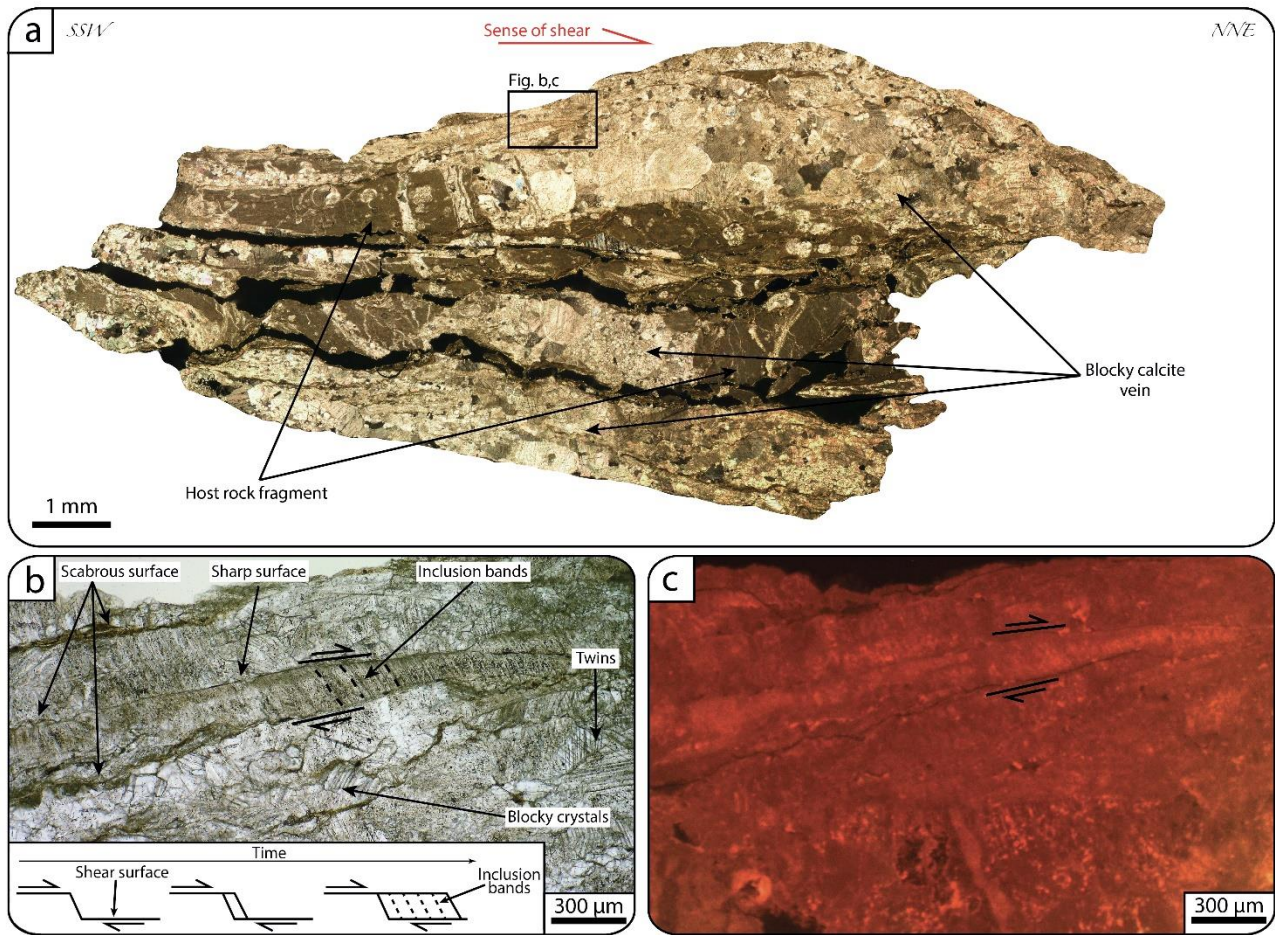
Figure 10. (a) Calcite slickenfiber along a C plane of K1 fabric (see Fig. 5a). Notice that the slickenfiber is mainly composed of blocky calcite veins and millimetric fragments of the host rock. (b) Detail of slickenfiber texture. Notice the twinned blocky veins bounded by scabrous surfaces and the rare calcite crystal layers bounded by sharp shear surfaces and with multiple inclusion bands at high angle with respect to the shear surfaces. In (b), it is shown a schematic representation of the typical model for the development of slickenfibers and inclusion bands by incremental dilation between shear surfaces. (c) Observation under cathodoluminescence light corresponding to (b) showing no marked differences in the colors of different generations of blocky calcite veins and slickenfiber.
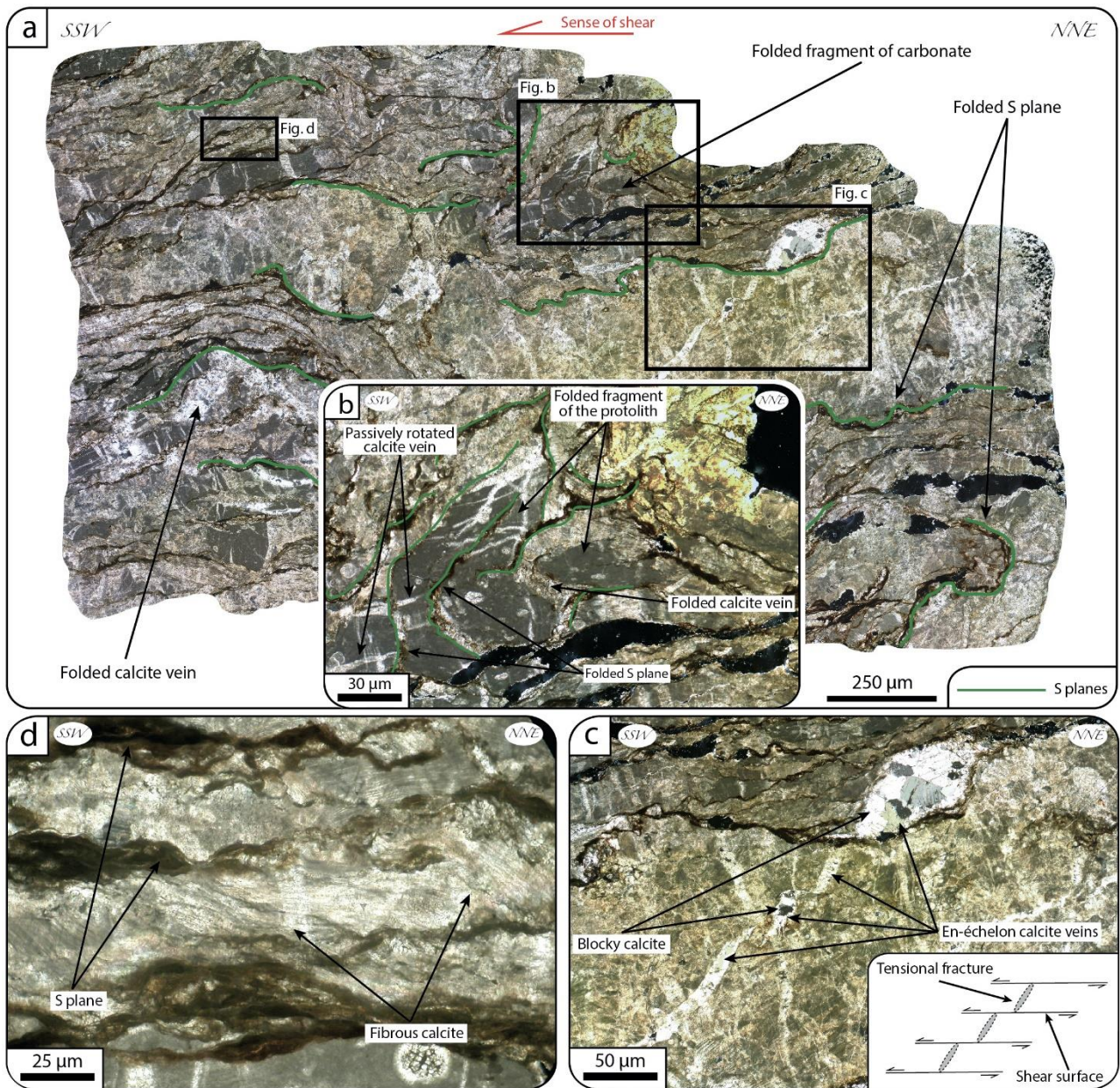
Figure 11. (a) Thin section of tectonites with folded S-C/C' fabric of K1 fabric. Calcite veins, dissolution planes and fragments of carbonates are widely affected by disharmonic folds. (b) Detail of folded fabric and passively rotated calcite veins. (c) En-échelon blocky calcite veins arranged consistently with a normal sense of shear (top-to-SSW). Inset in (b) shows the typical model for the development of en-échelon tensional fractures. (d) Fibrous calcite bounded by S planes and arranged parallel to the normal sense of shear.
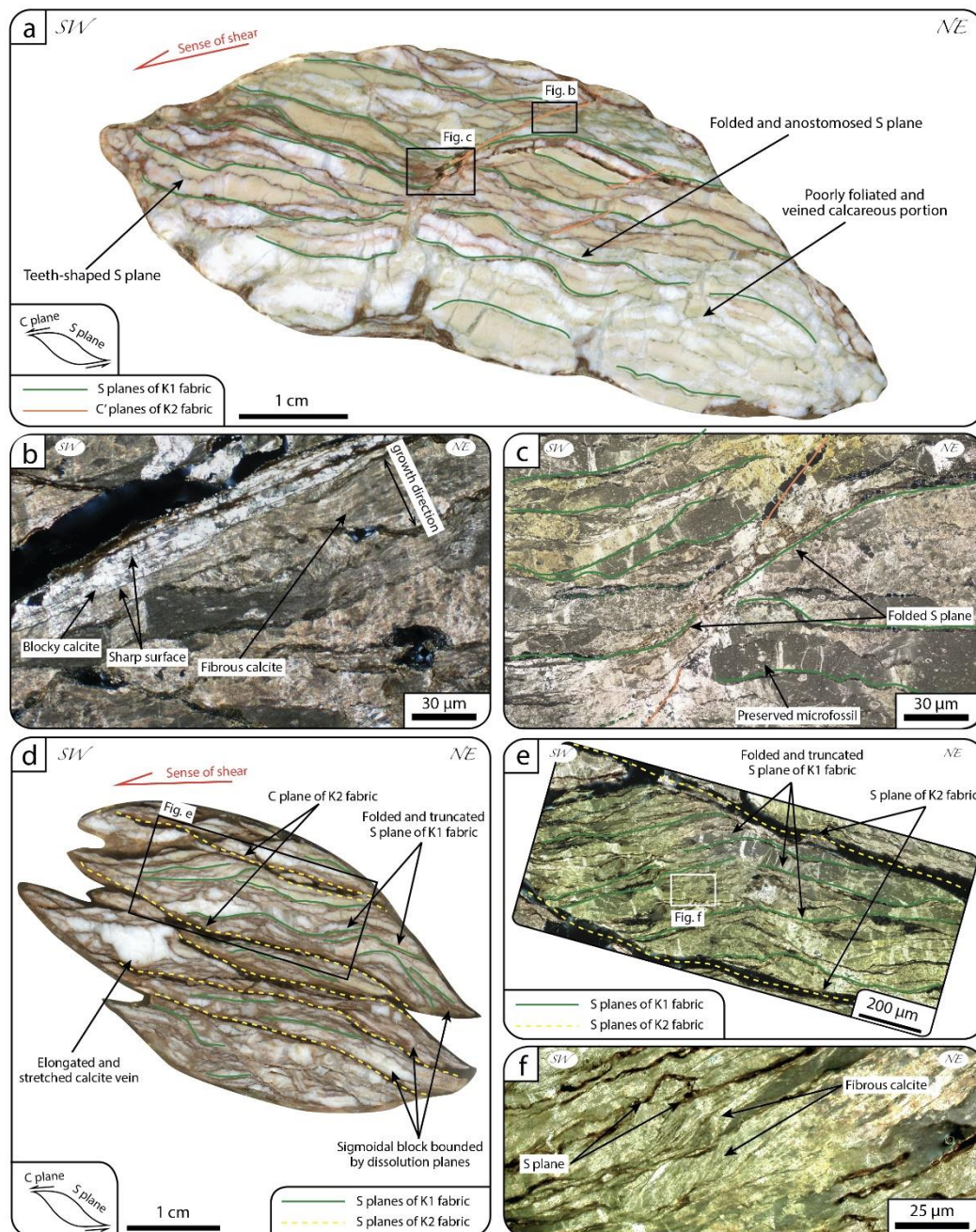
Figure 12. (a) High-resolution scan of a hand sample of a competent portion (consisting in a block with a sigmoidal shape) of K2 fabric. Anastomosed and folded S planes bound calcite mineralizations. C' planes are arranged at low angle with respect to the thrust surface (red arrow). (b) Detail of calcite mineralizations in proximity of C' planes. Blocky calcite veins bounded by sharp surfaces and fibrous calcite bounded by teeth-shaped dissolution planes. (c) Detail of C' planes and folded S planes. Notice the preserved microfossils and veins in the calcareous portion highlighted also within the microfabric of K1 fabric. (d) High-resolution scan of a hand sample and thin section of a highly-foliated portion within K2 fabric. Closely spaced dissolution planes bound calcareous sigmoids and calcite mineralizations. Calcareous sigmoids are internally deformed by folded dissolution S planes of K1 fabric truncated by NE-dipping S planes of K2 fabric. (e) Thin section showing the crosscutting relationship between dissolution S planes of K1 and K2 fabrics. Notice the preserved calcite veins highlighted in tectonites of K1 fabric. (f) Detail of calcite with fibrous habitus arranged parallel to the folded S planes of K1 fabric.
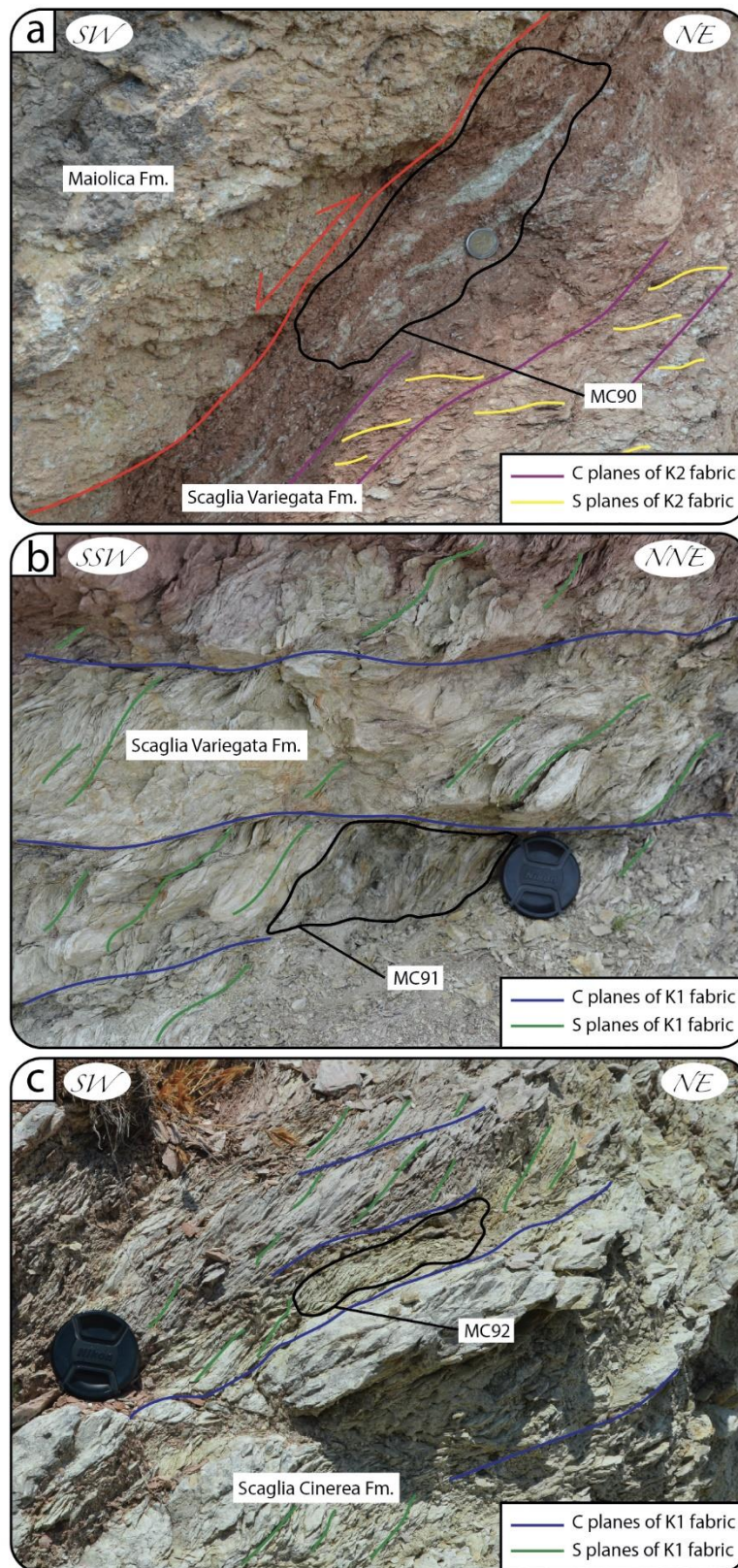
Figure 13. Sampling sites of the dated fault gouge collected within the shear zone of the MTT. (a) Sample MC 90 was collected within the shear zone in the first metres below the thrust surface showing extensional kinematics (K2 fabric). (b) Sample MC 91 was collected within the shear zone showing compressional kinematics (K1 fabric). (c) Sample MC92 was collected within the shear zone showing compressional kinematics (K1 fabric), in proximity of the splay which juxtaposes the Scaglia Variegata Fm. above the Scaglia Cinerea Fm. See figures 2, 3a, and 6a for the exact location of each sample.
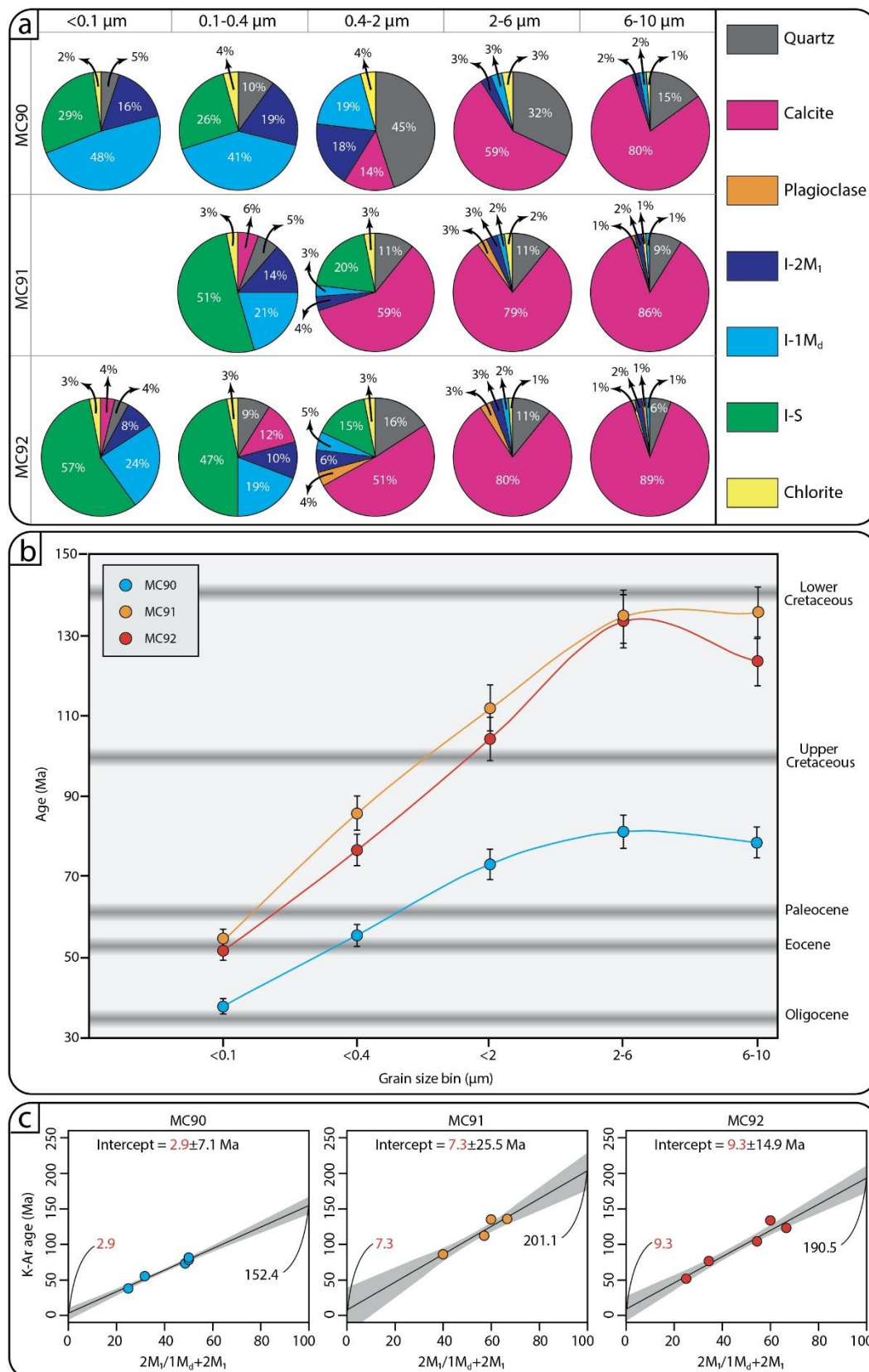
Figure 14. (a) X-ray semiquantitative analysis of clay gouges for samples MC90, MC91, and MC92. (b) K-Ar age versus grain size diagram. Dark grey horizontal bars define time periods of geological epochs. (c) Illite age analysis for the clay gouges. To estimate the ages of the authigenic illite-1M$_d$ end-member, which corresponds to the last faulting event recorded by the illite, we plotted K-Ar ages vs. percentage of illite-2M$_1$ (normalized to 100%) and linearly extrapolated to 0% illite-2M$_1$.
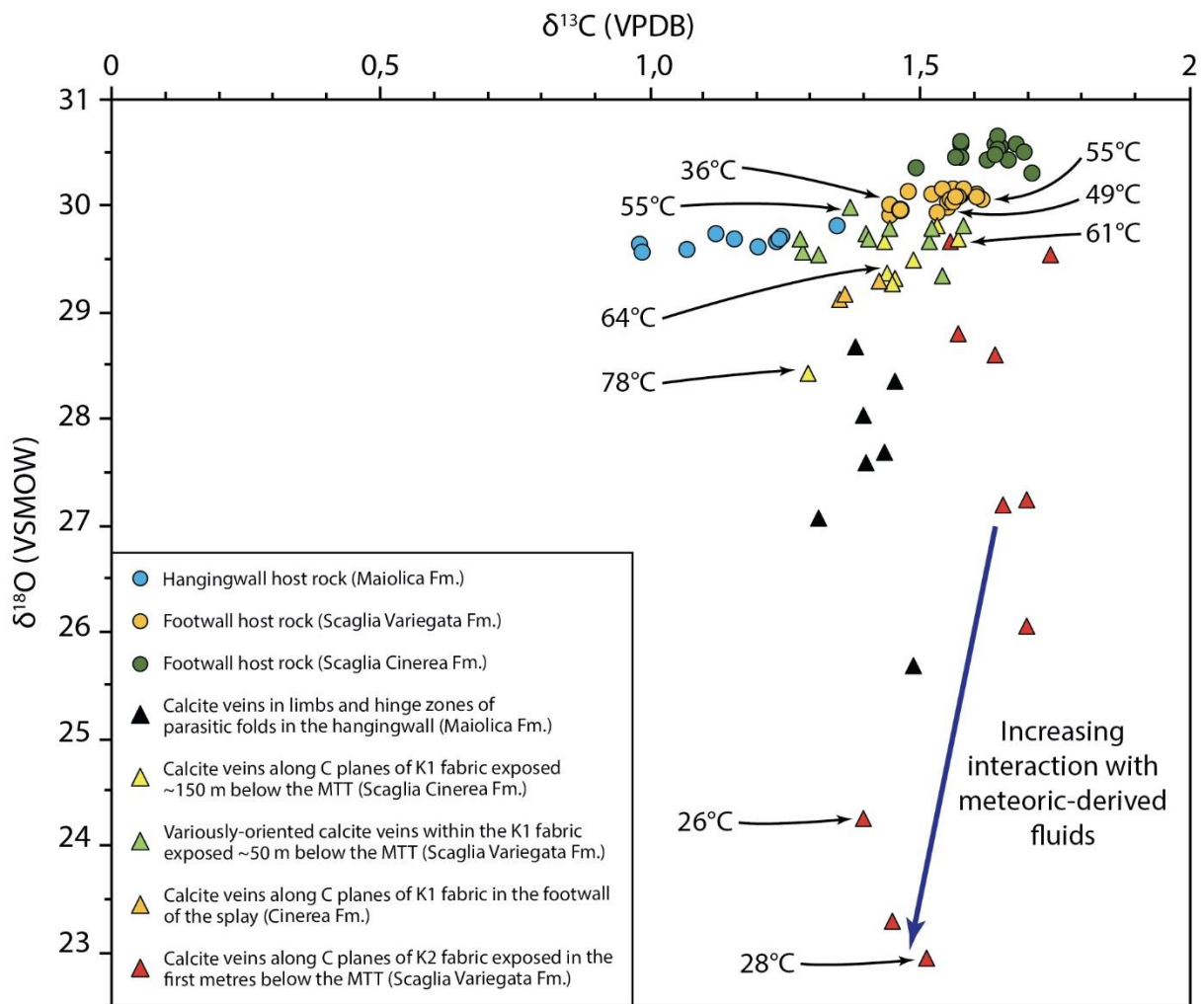
Figure 15. $\delta^{13}C$ (PDB) versus $\delta^{18}O$ (SMOW) diagram and clumped isotope temperature for calcite mineralizations (within the parasitic folds, K1 fabric, and K2 fabric) and host rocks.
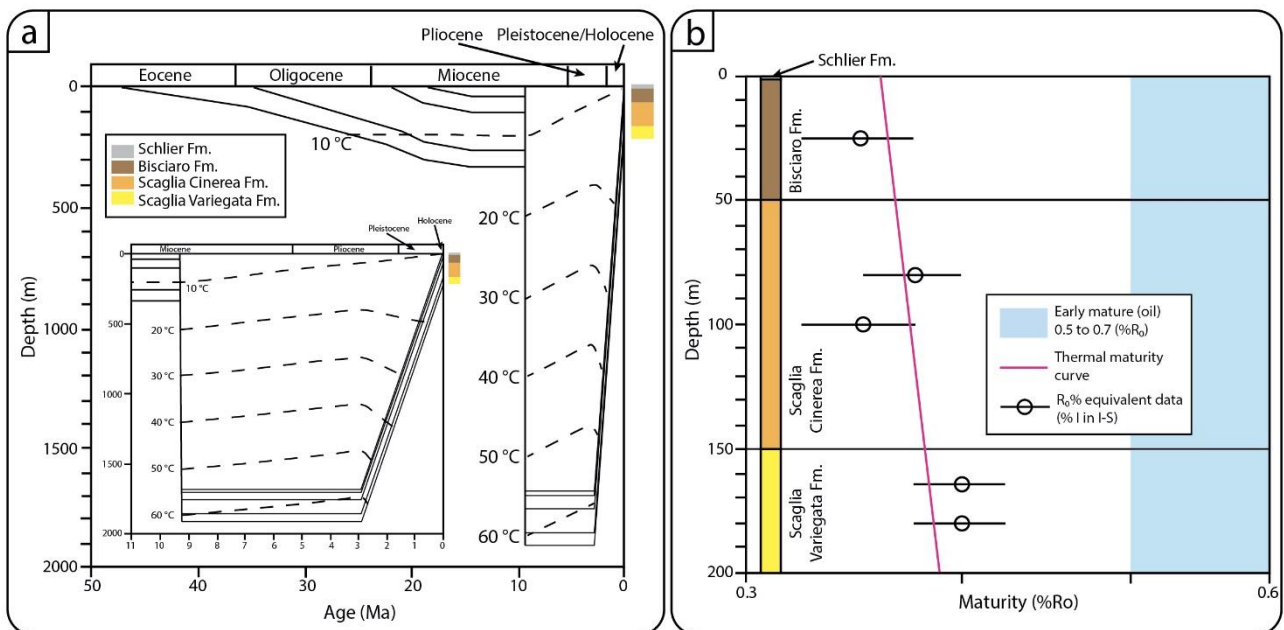

Figure 16. (a) Burial-exhumation history of the Eocene-Miocene sedimentary succession of the MTT with thrusting and exhumation constrained by K-Ar IAA ages. (b) Thermal maturity curve calibrated against illite content in mixed layers I-S.
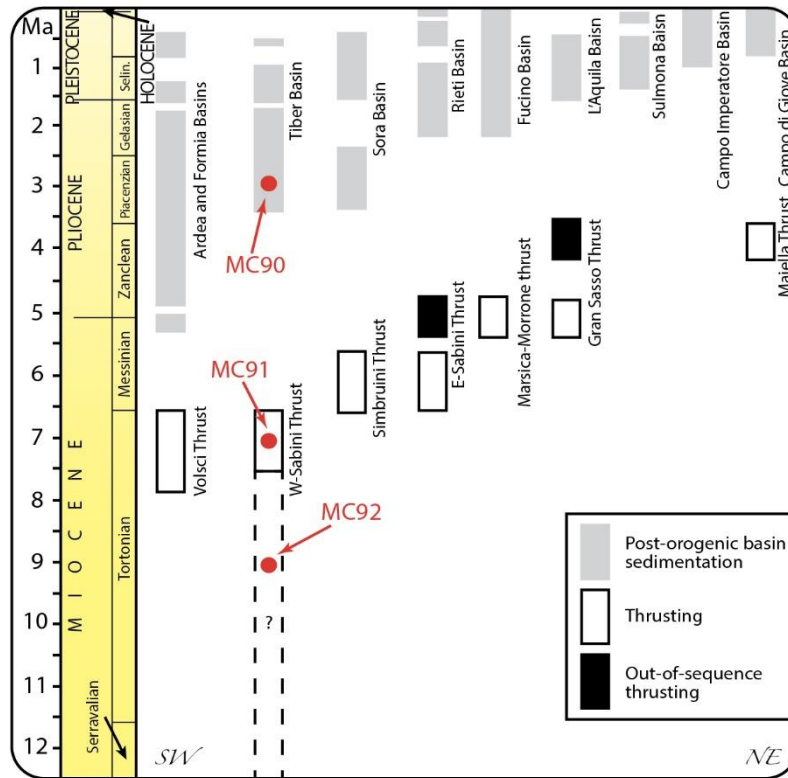
Figure 17. Time-distance diagram, including thrusting, out-of-sequence thrusting, and post-compressive basin sedimentation in the central Apennines (modified after Cavinato and DeCelles, 1999). The dashed rectangle is inferred from Cipollari and Cosentino. (1996), Cipollari et al. (1997), and Cosentino et al. (2014). Notice that K-Ar IAA ages (red dots) are consistent with the proposed temporal evolution of the western Sabine thrust belt.
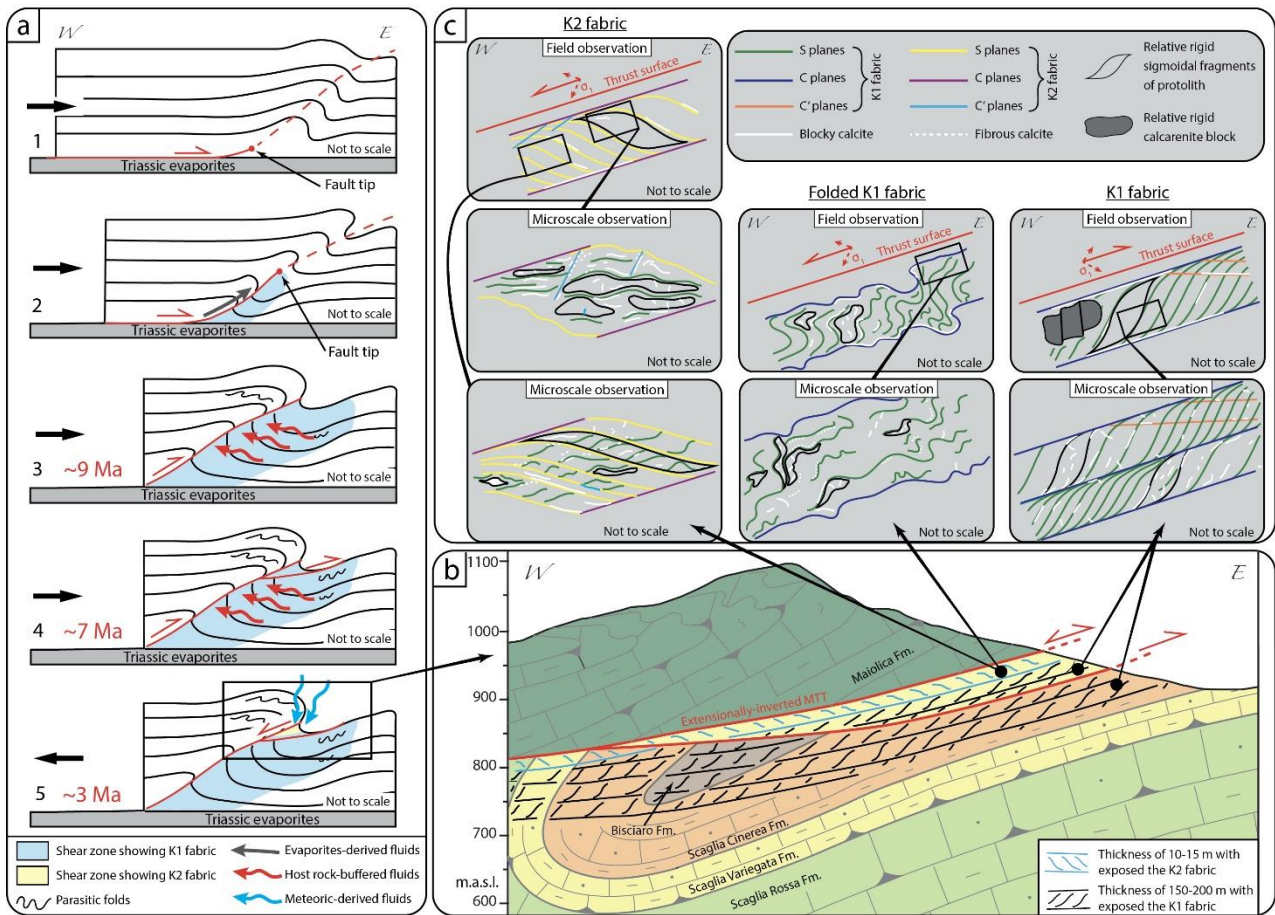
Figure 18. (a) Simplified conceptual model for the spatial-temporal and fluid-assisted tectonic evolution of the MTT. (b) Present-day schematic geometry of the whole structure of the Mt. Tancia area. The portions of the shear zone characterized by the K1 and K2 fabrics are shown. (c) Simplified reconstruction of folded and unfolded K1 fabric and K2 fabric observed in the field and by microscale observations.